

QUANTITATIVE UNIVERSAL APPROXIMATION FOR NOISY QUANTUM NEURAL NETWORKS

LUKAS GONON, ANTOINE JACQUIER, AND MARCEL MORDARSKI

ABSTRACT. We provide here a universal approximation theorem with precise quantitative error bounds for noisy quantum neural networks. We focus on applications to Quantitative Finance, where target functions are often given as expectations. We further provide a detailed numerical analysis, testing our results on actual noisy quantum hardware.

CONTENTS

1. Introduction	1
2. Quantum approximations of expectation functions	3
2.1. Notations and background	3
2.2. Extensions to expectation functions	3
2.3. Examples	5
3. Noisy Quantum neural networks	6
3.1. Background on Quantum operations	7
3.2. Noisy quantum circuit	7
3.3. Noisy probabilities	8
3.4. Noisy Quantitative Universal Approximation Theorem	9
3.5. Depolarising noise channel	11
3.6. Hardware-parameterised model for depolarising noise	14
3.7. Readout error in the depolarising case	17
4. Numerical experiments	17
4.1. Circuit architecture details	17
4.2. Gaussian density approximation	19
4.3. Black–Scholes Put option pricing: noiseless regime	21
4.4. Noise simulation	26
4.5. Hardware execution on <code>ibm_fez</code>	27
References	29

1. INTRODUCTION

Parameterised quantum circuits have emerged as a powerful paradigm for approximating high-dimensional functions. Mimicking classical Universal Approximation Theorems for

Date: April 3, 2026.

2020 Mathematics Subject Classification. 68Q12, 68T07, 65D15.

Key words and phrases. Universal Approximation Theorem, quantum neural networks, noise, NISQ.

AJ acknowledges financial support from the EPSRC grant EP/T032146/1. MM is funded through the UKRI DLA scholarship.

neural networks (see, for example, [4, 6, 12, 11, 14, 18, 39]), *qualitative* quantum versions of these theorems have recently appeared in [25, 26, 34]. Moreover, *quantitative* Universal Approximation Theorems, i.e., non-asymptotic error bounds – depending on circuit width, circuit depth and number of qubits – enable approximation of diverse classes of continuous functions, such as Korobov [2], Fourier-integrable [9, 10], Sobolev-space [20] and Hölder functions [40], provided an appropriate architectural choice of the quantum neural networks. These results, however, assume noiseless quantum circuits, which are not yet available in the current *noisy intermediate-scale quantum* (NISQ) environment. Even modest amounts of noise can radically modify the expected behaviours of the circuits: under non-unital noise, deep parameterised circuits estimating expectation values collapse to logarithmic depth [22], and (in this truncated regime) their outputs can be efficiently estimated on a classical computer for constant precision [21]. The existing approximation theorems therefore appear to be incompatible with the emerging theory of noisy circuits: they guarantee expressive power in a model that noise literature suggests is physically unattainable on near-term devices. Such issues may also limit the potential applicability of quantum neural networks, and one may instead ask the question:

Which functions remain representable, and with what accuracy, once realistic noise is introduced in the system?

Practitioners working under NISQ constraints have considered various approaches to modelling noise. On current hardware, uncorrected noise and decoherence set stringent depth budgets, barren plateaus make deep architectures hard to train, and naive transcriptions of expressive noiseless ansätze suffer dramatic performance losses [38, 17]. For example, the accuracy gap between noise-free simulation and execution on IBMQ devices can exceed 60% on simple classification tasks unless the model is explicitly made noise-aware [36]. A growing toolbox of noise-injection, post-measurement normalisation, and quantisation techniques has emerged precisely to patch this gap [37]. More recent “noise-aware QNN” architectures like NQNN [28] maintain classification accuracy under label and hardware noise by embedding noise attenuation directly into the variational ansatz. These results are, however, empirical and lack theoretical foundations to understand and mitigate risks due to noise.

In applied probability, notably in quantitative finance, typical target functions to compute are expectations of random processes (option prices, for example), in one or many dimensions (in the case of basket options) and both speed and accuracy are of primary importance. Classical tools rely on Monte Carlo techniques [7] or PDE methods [19] and are by now very well understood. With the (sometimes hyped) promise of increased speed, Quantum algorithms have recently entered this landscape: amplitude-estimation-based methods [35] and Quantum Monte Carlo [5] theoretically and asymptotically grant quadratic speedups, yet with assumptions beyond the allowed NISQ restrictions (large circuit depth, noiseless gates). A few NISQ-friendly proposals have attempted to address this (unary encodings [29], Black–Scholes reformulation as non-Hermitian evolution amendable to variational simulation [16]), but only offer empirical assessments, and rarely account for explicit hardware noise.

In this paper, we provide both a theoretical answer and hardware-specific numerical solutions to the above question for Fourier-integrable functions, as relevant, e.g., in quantitative finance. In Section 2, we extend the quantitative Universal Approximation Theorem for quantum neural networks developed in [9] to the case of functions given as expectations;

we further provide explicit bounds depending on the characteristics of the random variable under consideration and develop examples specific to Quantitative Finance. Section 3 focuses on the precise construction of the corresponding noisy quantum circuit (via quantum channels) and suggests methods to correct the noise. To make the results more explicit, we develop the case of depolarising noise, a common noise feature in NISQ settings. Finally, in Section 4, we detail numerical experiments focusing on option pricing in the Black-Scholes model and relate precisely the theoretical noise above to real hardware noise.

2. QUANTUM APPROXIMATIONS OF EXPECTATION FUNCTIONS

In this section, we prove a quantitative Universal Approximation Theorem, providing error bounds for quantum neural network approximations to expectation functions, as relevant, e.g., in quantitative finance. We consider quantum neural networks as in [9], which were also implemented in [3] on Rydberg atom array.

2.1. Notations and background. We recall the following spaces introduced in [9]:

$$\begin{aligned}\mathcal{F} &:= \left\{ f : \mathbb{R}^d \rightarrow \mathbb{R} : f \in \mathcal{C}(\mathbb{R}^d) \cap L^1(\mathbb{R}^d) \right\}, \\ \mathcal{F}_R &:= \left\{ f \in \mathcal{F}, \text{ with } L^1[\widehat{f}] \leq R \right\}, \quad \text{for any } R > 0.\end{aligned}\tag{2.1}$$

Here, we denote the Fourier transform $\widehat{f}(\boldsymbol{\xi}) := \int_{\mathbb{R}^d} e^{-2i\pi\boldsymbol{x}\cdot\boldsymbol{\xi}} f(\boldsymbol{x}) d\boldsymbol{x}$, $\boldsymbol{\xi} \in \mathbb{R}^d$, and $L^1[\widehat{f}] := \int_{\mathbb{R}^d} |\widehat{f}(\boldsymbol{\xi})| d\boldsymbol{\xi}$ (which may be infinite in general, but is finite for $f \in \mathcal{F}$).

Gonon and Jacquier [9] showed that a function $f \in \mathcal{F}_R$ may be approximated by (the output of) a quantum neural network (QNN) up to accuracy at least ε using $\mathcal{O}(\lceil \log_2(\varepsilon^{-1}) \rceil)$ qubits. More specifically, let $f_{n,\boldsymbol{\theta}}^R$ the function defined as

$$f_{n,\boldsymbol{\theta}}^R(\cdot) := R \left\{ 1 - 2 \left(\mathbb{P}_1 + \mathbb{P}_2 \right) \right\},\tag{2.2}$$

with $\mathbb{P}_1, \mathbb{P}_2$ the output probability of a specific parameterised quantum circuit (or quantum neural network – QNN) as specified in [9, Section II.B]. Here $\boldsymbol{\theta} \in \boldsymbol{\Theta}$ denotes the parameters of the QNN and $n \in \mathbb{N}$ the accuracy parameter, related to the number of qubits \mathbf{n} via $\mathbf{n} = \lceil \log_2(4n + n_0) \rceil$. The probabilities \mathbb{P}_1 and \mathbb{P}_2 depend on $\boldsymbol{\theta}$ and the input variable of $f_{n,\boldsymbol{\theta}}^R(\cdot)$, but we omit the dependence for notational conciseness.

We shall be considering the following statement, where from now on, μ denotes a fixed probability measure on \mathbb{R}^d that can be chosen arbitrarily:

Statement 2.1. *It holds that $L^1[\widehat{f}] < \infty$ and there exists $\mathfrak{B} > 0$ such that, for any $n \in \mathbb{N}$, $R \geq L^1[\widehat{f}]$, there exists $\boldsymbol{\theta} \in \boldsymbol{\Theta}$ such that*

$$\left(\int_{\mathbb{R}^d} |f(\boldsymbol{x}) - f_{n,\boldsymbol{\theta}}^R(\boldsymbol{x})|^2 \mu(d\boldsymbol{x}) \right)^{1/2} \leq \frac{\mathfrak{B}}{\sqrt{n}}.$$

In particular, [9, Theorem II.4] showed that this statement holds for $f \in \mathcal{F}_R$ with $\mathfrak{B} = L^1[\widehat{f}]$. The remainder of this section is devoted to extending this result to the specific context of expectation functions.

2.2. Extensions to expectation functions. We start with the following case, which leverages the results in [9].

Proposition 2.2. *Let L be an \mathbb{R}^d -valued random variable and $f(\boldsymbol{x}) := \mathbb{E}[\Phi_1(\boldsymbol{x} + L)]$ on \mathbb{R}^d . If $\Phi_1 \in L^1(\mathbb{R}^d)$ and $\boldsymbol{\xi} \mapsto \mathbb{E}[e^{iL\cdot\boldsymbol{\xi}}]$ is integrable, then Statement 2.1 holds with $\mathfrak{B} = L^1[\widehat{f}]$.*

Proof. First, we aim to show that f and \widehat{f} are integrable. By change-of-variable, the characteristic function $\boldsymbol{\xi} \mapsto \mathbb{E}[e^{-iL \cdot \boldsymbol{\xi}}]$ of $-L$ is integrable. Hence, by [32, Proposition 2.5(xii)] the random variable $-L$ has a bounded, continuous density g with respect to the Lebesgue measure and we may write $f(\mathbf{x}) = \int_{\mathbb{R}^d} \Phi_1(\mathbf{x} - \mathbf{y})g(\mathbf{y})d\mathbf{y} = (\Phi_1 * g)(\mathbf{x})$. In particular, this implies that f is integrable, since both g and Φ_1 are integrable. Next, we show that \widehat{f} is integrable. The convolution theorem yields $\widehat{f}(\boldsymbol{\xi}) = \widehat{\Phi}_1(\boldsymbol{\xi})\widehat{g}(\boldsymbol{\xi})$. Inserting the definition of g , we may represent $\widehat{g}(\boldsymbol{\xi}) = \int_{\mathbb{R}^d} e^{-i\mathbf{x} \cdot \boldsymbol{\xi}}g(\mathbf{x})d\mathbf{x} = \mathbb{E}[e^{-i\boldsymbol{\xi} \cdot (-L)}]$. Hence, $\widehat{f}(\boldsymbol{\xi}) = \widehat{\Phi}_1(\boldsymbol{\xi})\widehat{g}(\boldsymbol{\xi}) = \widehat{\Phi}_1(\boldsymbol{\xi})\mathbb{E}[e^{i\boldsymbol{\xi} \cdot L}]$ is integrable, since (i) $\widehat{\Phi}_1$ is bounded due to $\Phi_1 \in L^1(\mathbb{R}^d)$ and (ii) $\boldsymbol{\xi} \mapsto \mathbb{E}[e^{i\boldsymbol{\xi} \cdot L}]$ is integrable. Since f and \widehat{f} are both integrable, [9, Theorem II.4] hence implies that for any $n \in \mathbb{N}$, there exists $\boldsymbol{\theta} \in \Theta$ such that

$$\left(\int_{\mathbb{R}^d} |f(\mathbf{x}) - f_{n,\boldsymbol{\theta}}^R(\mathbf{x})|^2 \mu(d\mathbf{x}) \right)^{1/2} \leq \frac{L^1[\widehat{f}]}{\sqrt{n}}$$

for any choice of R such that $L^1[\widehat{f}] \leq R$. \square

As a special case, consider an exponential Lévy model, so that $L = (L_t)_{t \geq 0}$ is a d -dimensional Lévy process with characteristic triplet (Σ, γ, ν) , where the $d \times d$ symmetric non-negative definite matrix Σ denotes the diffusion matrix, $\gamma \in \mathbb{R}^d$ is the drift and ν a measure on \mathbb{R}^d satisfying $\nu(\{0\}) = 0$ and $\int_{\mathbb{R}^d} (1 \wedge |\mathbf{x}^2|)\nu(d\mathbf{x}) < \infty$. We refer the reader to [32, Chapters 1-2] for details about such processes.

Then $f(\mathbf{x}) = \mathbb{E}[\Phi(e^{\mathbf{x} + L_T})]$ corresponds to the price of a European option with payoff Φ and maturity T in an exponential Lévy model with d underlying asset prices modelled by $S_t = S_0 e^{L_t}$ for $S_0 = e^{\mathbf{x}}$, where the drift γ is chosen such that e^L is a martingale. For $\nu = 0$, $d = 1$ and $\gamma = -\frac{1}{2}\Sigma$, this corresponds precisely to the Black-Scholes model. The next corollary shows that Proposition 2.2 can be directly applied to such models, with $\Phi_1 = \Phi \circ \exp$.

Corollary 2.3. *Let L be a d -dimensional Lévy process such that $\boldsymbol{\xi} \mapsto \mathbb{E}[e^{iL_T \cdot \boldsymbol{\xi}}]$ is integrable. Let $f(\mathbf{x}) = \mathbb{E}[\Phi(e^{\mathbf{x} + L_T})]$, $\mathbf{x} \in \mathbb{R}^d$ and assume $\Phi \circ \exp \in L^1(\mathbb{R}^d)$. Then Statement 2.1 holds with $\mathfrak{B} = L^1[\widehat{f}]$.*

The next corollary provides sufficient conditions ensuring that the integrability conditions on the characteristic functions are satisfied. The integrability conditions on the payoff Φ are satisfied, for example, if Φ is a butterfly basket option or a capped Call or Put option.

Corollary 2.4. *Let L be a d -dimensional Lévy process with non-degenerate diffusion matrix: there exists $C > 0$ such that $\frac{1}{2}\boldsymbol{\xi} \cdot \Sigma \boldsymbol{\xi} \geq C\|\boldsymbol{\xi}\|^2$ for all $\boldsymbol{\xi} \in \mathbb{R}^d$. Let $f(\mathbf{x}) = \mathbb{E}[\Phi(e^{\mathbf{x} + L_T})]$, $\mathbf{x} \in \mathbb{R}^d$ and assume $\Phi \circ \exp \in L^1(\mathbb{R}^d)$. Then Statement 2.1 holds with $\mathfrak{B} = \|\Phi \circ \exp\|_{L^1(\mathbb{R}^d)} \left(\frac{2\pi}{CT}\right)^{d/2}$.*

Proof. By the same argument as in the proof of [8, Theorem 13], it follows that $|\mathbb{E}[e^{iL_T \cdot \boldsymbol{\xi}}]| \leq \exp\{-CT\|\boldsymbol{\xi}\|^2\}$. In particular, $\boldsymbol{\xi} \mapsto \mathbb{E}[e^{iL_T \cdot \boldsymbol{\xi}}]$ is integrable. Moreover, with $\Phi_1 = \Phi \circ \exp$ and using the representation $\widehat{f}(\boldsymbol{\xi}) = \widehat{\Phi}_1(\boldsymbol{\xi})\mathbb{E}[e^{i\boldsymbol{\xi} \cdot L_T}]$ from the proof of Proposition 2.2, we can bound $L^1[\widehat{f}]$ as follows:

$$\begin{aligned} L^1[\widehat{f}] &= \int_{\mathbb{R}^d} |\widehat{f}(\boldsymbol{\xi})|d\boldsymbol{\xi} \leq \|\Phi_1\|_{L^1(\mathbb{R}^d)} \int_{\mathbb{R}^d} |\mathbb{E}[e^{iL_T \cdot \boldsymbol{\xi}}]|d\boldsymbol{\xi} \leq \|\Phi_1\|_{L^1(\mathbb{R}^d)} \int_{\mathbb{R}^d} e^{-CT\|\boldsymbol{\xi}\|^2}d\boldsymbol{\xi} \\ &= \|\Phi_1\|_{L^1(\mathbb{R}^d)} \left| \frac{2\pi}{CT} \right|^{\frac{d}{2}}, \end{aligned}$$

since the density of a $\mathcal{N}_d(0, 1_{d \times d}(CT)^{-1})$ -distribution integrates to 1. \square

2.3. Examples.

2.3.1. *Gaussian density.* Consider the one-dimensional Gaussian density

$$f_\sigma(x) = \frac{1}{\sigma\sqrt{2\pi}} \exp\left\{-\frac{x^2}{2\sigma^2}\right\}, \quad x \in \mathbb{R},$$

given some $\sigma > 0$, so that its Fourier transform simply reads $\widehat{f}_\sigma(\xi) = e^{-2\pi^2\sigma^2\xi^2}$ for all $\xi \in \mathbb{R}$ and a direct computation yields $L^1[\widehat{f}_\sigma] = \frac{1}{\sigma\sqrt{2\pi}}$.

2.3.2. *Put option in the Bachelier model.* The same reasoning also applies to standard (arithmetic) Lévy models $f(\mathbf{x}) = \mathbb{E}[\Phi_1(\mathbf{x} + L_T)]$, $\mathbf{x} \in \mathbb{R}^d$ with $\Phi_1 \in L^1(\mathbb{R}^d)$. For example, consider the Bachelier model with volatility $\sigma > 0$, under which the stock price process satisfies $S_t = S_0 + \sigma W_t$, for some standard Brownian motion W . In this case, from Corollary 2.4 with $C = \frac{1}{2}\sigma^2$, then Statement 2.1 holds with $\mathfrak{B} = \|\Phi_1\|_{L^1(\mathbb{R})} \frac{2\sqrt{\pi}}{\sigma\sqrt{T}}$. For example, if $\Phi_1(x) = (K - x)^+ \mathbb{1}_{\{x \geq 0\}}$ is the payoff of a Put option (defined on the whole real line), then $\|\Phi_1\|_{L^1(\mathbb{R})} = \int_0^K (K - x)dx = \frac{K^2}{2}$ and hence $\mathfrak{B} = \frac{\sqrt{\pi}K^2}{\sigma\sqrt{T}}$. We can however get a sharper bound by directly computing the Fourier transform $\widehat{\Phi}_1(\xi) = \frac{K}{2i\pi\xi} + \frac{1 - e^{-2i\pi K\xi}}{(2\pi\xi)^2}$ by integration by parts. Since $|e^{iu} - 1| \leq |u|$, then $|\widehat{\Phi}_1(\xi)| \leq \frac{K}{\pi|\xi|}$ for $|\xi| > 0$. Moreover, $|e^{-iu} - 1 + iu| \leq \frac{1}{2}|u|^2$ for all $u \in \mathbb{R}$ and thus $|\widehat{\Phi}_1(\xi)| = \left| \frac{-1 + e^{-2i\pi K\xi} + 2i\pi\xi K}{(2\pi\xi)^2} \right| \leq \frac{K^2}{2}$. Splitting the integral and inserting these bounds, we obtain, for any $a > 0$,

$$\begin{aligned} L^1[\widehat{f}] &= \int_{\mathbb{R}} |\widehat{\Phi}_1(\xi)| |\mathbb{E}[e^{iL_T \cdot \xi}]| d\xi \\ &\leq \int_{-1/a}^{1/a} \frac{K^2}{2} e^{-\frac{1}{2}\sigma^2 T \xi^2} d\xi + 2 \int_{1/a}^{\infty} \frac{K}{\pi|\xi|} e^{-\frac{1}{2}\sigma^2 T \xi^2} d\xi \\ &= K^2 \frac{\sqrt{\pi}}{\sigma\sqrt{2T}} \operatorname{erf}\left(\frac{\sigma\sqrt{T}}{a\sqrt{2}}\right) + \frac{K}{\pi} E_1\left(\frac{\sigma^2 T}{2a^2}\right) =: \mathfrak{B}(a), \end{aligned}$$

where $E_1(z) := \int_z^{\infty} x^{-1} e^{-x} dx$ denotes the exponential integral and $\operatorname{erf}(\cdot)$ the error function. Since $\partial_z \operatorname{erf}(z) = \frac{2}{\sqrt{\pi}} e^{-z^2}$ and $\partial_z E_1(z) = -z^{-1} e^{-z}$, then

$$\partial_a \mathfrak{B}(a) = \frac{2a - K\pi}{a^2\pi} K \exp\left\{-\frac{\sigma^2 T}{2a^2}\right\},$$

and thus $\mathfrak{B}(\cdot)$ is decreasing on $(0, \frac{K\pi}{2})$ and increasing on $(\frac{K\pi}{2}, \infty)$, with minimum attained at $\frac{K\pi}{2}$, so the best upper bound is $\mathfrak{B} = \mathfrak{B}(\frac{K\pi}{2})$. Working with quantities normalised by the spot price, for example we obtain for $K = 1$, $\sigma = 0.2$, $T = 1$ and $a = K\pi/2$ then $\mathfrak{B} \approx 0.1986$.

2.3.3. *Black-Scholes.* In the Black-Scholes model, the stock price (assuming no interest rate) is the unique strong solution to the stochastic differential equation $dS_t = \sigma S_t dW_t$ starting from $S_0 > 0$. The European Put price with maturity $T > 0$ and strike $K > 0$ then reads

$$\operatorname{Put}_{\text{BS}}(S_0, K, T, r, \sigma) = K\mathcal{N}(-d_-) - S_0\mathcal{N}(-d_+),$$

with $\mathcal{N}(\cdot)$ the Gaussian cumulative distribution function and $d_{\pm} := \frac{\log(S_0/K)}{\sigma\sqrt{T}} \pm \frac{1}{2}\sigma\sqrt{T}$.

Truncated Put option in Black-Scholes. Fix $\underline{K} \in (0, K)$ and consider the Black-Scholes model, that is $f(x) = \mathbb{E}[\Phi_1(x + L_T)]$, $x \in \mathbb{R}$ and $\Phi_1 = \Phi \circ \exp$ with $\Phi(x) = (K - x)_+ \mathbb{1}_{\{x \geq \underline{K}\}}$. Now,

$$\|\Phi_1\|_{L^1(\mathbb{R})} = \int_{\mathbb{R}} (K - e^x)_+ \mathbb{1}_{\{e^x \geq \underline{K}\}} dx = \int_{\log(\underline{K})}^{\log(K)} (K - e^x) dx = K(\log(K) - \log(\underline{K})) - (K - \underline{K}),$$

which is finite. Thus, Corollary 2.4 with $C = \frac{1}{2}\sigma^2$ yields that Statement 2.1 holds with $\mathfrak{B} = [K(\log(K) - \log(\underline{K})) - (K - \underline{K})] \frac{2\sqrt{\pi}}{\sigma\sqrt{T}}$. We can obtain a sharper bound by directly computing the Fourier transform $\widehat{\Phi}_1(\xi) = \int_{-\underline{k}}^k (K - e^x) e^{-2i\pi x\xi} dx$, where we write $\underline{k} = \log(\underline{K})$ and $k = \log(K)$. We obtain

$$\widehat{\Phi}_1(\xi) = \frac{K}{-2i\pi\xi} (e^{-2i\pi k\xi} - e^{-2i\pi \xi}) + \frac{1}{-2i\pi\xi + 1} (e^{(-2i\pi\xi+1)k} - e^{(-2i\pi\xi+1)\underline{k}}),$$

and therefore

$$|\widehat{\Phi}_1(\xi)| \leq \frac{K}{\pi|\xi|} + \frac{1}{\sqrt{1 + 4\pi^2\xi^2}} (K + \underline{K}) \leq \frac{3K + \underline{K}}{2\pi|\xi|}$$

and $|\widehat{\Phi}_1(\xi)| \leq \|\Phi_1\|_{L^1(\mathbb{R})}$. Thus, we may estimate, for any $a > 0$,

$$\begin{aligned} L^1[\widehat{f}] &= \int_{\mathbb{R}} |\widehat{\Phi}_1(\xi)| |\mathbb{E}[e^{iL_T \cdot \xi}]| d\xi \\ &\leq \int_{-1/a}^{1/a} [K(k - \bar{k}) - (K - \underline{K})] e^{-\frac{1}{2}\sigma^2 T \xi^2} d\xi + 2 \int_{1/a}^{\infty} \frac{3K + \underline{K}}{2\pi|\xi|} e^{-\frac{1}{2}\sigma^2 T \xi^2} d\xi \\ &= 2[K(\log(K) - \log(\underline{K})) - (K - \underline{K})] \frac{\sqrt{\pi}}{\sigma\sqrt{2T}} \operatorname{erf}\left(\frac{\sigma\sqrt{T}}{a\sqrt{2}}\right) + \frac{3K + \underline{K}}{2\pi} E_1\left(\frac{\sigma^2 T}{2a^2}\right) =: \mathfrak{B}(a). \end{aligned}$$

Analogously as in the previous example, we may verify that $\mathfrak{B}(a)$ attains its minimum at $a^* = \frac{2[K(\log(K) - \log(\underline{K})) - (K - \underline{K})]\pi}{(3K + \underline{K})}$. For $K = 1$, $\underline{K} = 0.4$, $\sigma = 0.2$, $T = 1$ and $a = a^* \approx 0.584$ we obtain $\mathfrak{B} \approx 2.316$.

Put option in Black-Scholes. For a Put option in a Black-Scholes model, we can then apply the bound from Example 2.3.3 and combine it with a truncation estimate. Let $f_i(x) = \mathbb{E}[\Phi_i(x + L_T)]$, $x \in \mathbb{R}$ with Φ_1 as in the (truncated) previous example and $\Phi_2 = \Phi \circ \exp$ with $\Phi(x) = (K - x)_+$. Then f_2 is the true Put price and f_1 can be approximated using a QNN with bound given in the previous example and we can estimate the difference

$$\begin{aligned} |f_1(x) - f_2(x)| &= \left| \mathbb{E} \left[(K - e^{x+L_T})_+ \mathbb{1}_{\{e^{x+L_T} \leq \underline{K}\}} \right] \right| \leq K \mathbb{P}(L_T < \log(\underline{K}) - x) \\ &= K \mathbb{P} \left(Z \leq \frac{\log(\underline{K}) - x + \frac{\sigma^2 T}{2}}{\sigma\sqrt{T}} \right), \end{aligned}$$

where $Z \sim \mathcal{N}(0, 1)$. For example, at the money ($x = 0$) and for $K = 1$, $\underline{K} = 0.4$, $\sigma = 0.2$, $T = 1$ we obtain an error of $\approx 4 \cdot 10^{-6}$.

3. NOISY QUANTUM NEURAL NETWORKS

In this section, we develop quantitative Universal Approximation Theorems for noisy quantum neural networks. These results apply both to the Fourier-integrable functions in (2.1) and to expectation functions, as considered in Section 2.2. In particular, the results apply to the Black-Scholes model.

We start with the setup considered in [9, Section 2], where a quantum circuit evolves the initial quantum state to the output state. To account for noise in physical quantum hardware, this setup must be translated to a density operator formalism. In the wavefunction formalism of [9], the initial state is $|0\rangle^{\otimes n}$, where n is the number of qubits. In the density operator formalism, this corresponds to the pure state density matrix

$$\rho_0 = |0\rangle\langle 0|^{\otimes n}.$$

This state is then evolved to

$$\rho_1 = \mathbf{V}\rho_0\mathbf{V}^\dagger \quad \text{and} \quad \rho_2 = \mathbf{U}(\boldsymbol{\theta}, \mathbf{x})\rho_1\mathbf{U}^\dagger(\boldsymbol{\theta}, \mathbf{x}), \quad (3.1)$$

for some unitary operators \mathbf{V} and \mathbf{U} , the latter being a function of parameters $\boldsymbol{\theta}$ and inputs \mathbf{x} . To add noise in the system, we require operations more general than simple unitary matrix multiplications, namely quantum channels, which we now recall briefly and refer the reader to [33, Section 3.5] for full details.

3.1. Background on Quantum operations. Let \mathcal{H} be a finite-dimensional Hilbert space and denote

$$\mathcal{D}(\mathcal{H}) := \left\{ \rho \in \mathcal{H} : \rho^\dagger = \rho, \rho \geq 0, \text{Tr}[\rho] = 1 \right\},$$

the space of density matrices with trace equal to one.

Definition 3.1. A quantum channel Ψ is a completely positive trace-preserving (CPTP) convex-linear map from $\mathcal{D}(\mathcal{H})$ to $\mathcal{D}(\mathcal{H})$.

The *completely positive* property means that any extension $\Psi \otimes \mathbf{I}$ is also a positive map, where \mathbf{I} is the identity operator of any (finite) dimension. The following result, due to Kraus [15] gives a useful characterisation of quantum channels:

Proposition 3.2. For a given quantum channel $\Psi : \mathcal{D}(\mathcal{H}) \rightarrow \mathcal{D}(\mathcal{H})$, there exists a sequence of linear maps $\{K_\ell\}_\ell$, called the Kraus operators, such that the operator-sum representation

$$\Psi(\rho) = \sum_\ell K_\ell \rho K_\ell^\dagger$$

holds for all $\rho \in \mathcal{D}(\mathcal{H})$, with $\sum_\ell K_\ell K_\ell^\dagger = \mathbf{I}$. The sums over ℓ run from 1 to some constant smaller or equal than $\dim(\mathcal{H})^2$.

In case there is only one Kraus operator, say K_1 , then the decomposition reads $\Psi(\rho) = K_1 \rho K_1^\dagger$, with the completeness relation $K_1 K_1^\dagger = \mathbf{I}$. In this case, K_1 is either unitary or a scaled unitary of the form $\alpha \mathbf{U}$, with $|\alpha| = 1$ and \mathbf{U} unitary, reducing this computation to the standard (noiseless) quantum evolution.

3.2. Noisy quantum circuit. We now consider a general quantum channel Ψ , as per Definition 3.1, with Kraus representation

$$\Psi(\rho) = \sum_k K_k \rho K_k^\dagger,$$

where $\{K_k\}_k$ are Kraus operators satisfying the completeness relation $\sum_k K_k^\dagger K_k = \mathbf{I}$. The noisy version of (3.1) reads

$$\tilde{\rho}_2 = \Psi_{\mathbf{U}}\left(\mathbf{U}(\boldsymbol{\theta}, \mathbf{x})\Psi_{\mathbf{V}}\left(\mathbf{V}\rho_0\mathbf{V}^\dagger\right)\mathbf{U}^\dagger(\boldsymbol{\theta}, \mathbf{x})\right) = \Psi_{\mathbf{U}}\left(\mathbf{U}(\boldsymbol{\theta}, \mathbf{x})\Psi_{\mathbf{V}}(\rho_1)\mathbf{U}^\dagger(\boldsymbol{\theta}, \mathbf{x})\right) \quad (3.2)$$

where Ψ_V and Ψ_U represent the noise channels respectively associated with V and U and ρ_1 is the noiseless quantum state (as a density operator) after the first layer as in (3.1). Using $|\psi_1\rangle = \frac{1}{\sqrt{n}} \sum_{i=0}^{n-1} |4i\rangle$ from [9], where n is such that $\mathbf{n} = \lceil \log_2(4n) \rceil$, then

$$\rho_1 = |\psi_1\rangle\langle\psi_1| = \frac{1}{n} \sum_{i=0}^{n-1} \sum_{j=0}^{n-1} |4i\rangle\langle 4j|.$$

The general noisy state is therefore

$$\tilde{\rho}_2 = \frac{1}{n} \sum_k \sum_\ell \sum_{i=0}^{n-1} \sum_{j=0}^{n-1} K_k^U(\boldsymbol{\theta}, \mathbf{x}) K_\ell^V |4i\rangle\langle 4j| K_\ell^{V\dagger} U^\dagger(\boldsymbol{\theta}, \mathbf{x}) K_k^{U\dagger}. \quad (3.3)$$

Remark 3.3 (Pure state decomposition). The noisy density state $\tilde{\rho}_2$ can be re-expressed as a wavefunction through a convex combination of pure states. For each pair of Kraus indices (k, ℓ) , the quantum state

$$|\tilde{\phi}_{k,\ell}\rangle := K_k^U(\boldsymbol{\theta}, \mathbf{x}) K_\ell^V |\psi_1\rangle,$$

is not normalised, since $\langle\tilde{\phi}_{k,\ell}|\tilde{\phi}_{k,\ell}\rangle$ is not necessarily equal to one as each individual Kraus operator is not unitary. We define its normalised version $|\phi_{k,\ell}\rangle := \frac{1}{\sqrt{p_{k,\ell}}} |\tilde{\phi}_{k,\ell}\rangle$, with $p_{k,\ell} := \langle\tilde{\phi}_{k,\ell}|\tilde{\phi}_{k,\ell}\rangle$ and therefore

$$\tilde{\rho}_2 = \sum_{k,\ell} |\tilde{\phi}_{k,\ell}\rangle\langle\tilde{\phi}_{k,\ell}| = \sum_{k,\ell} p_{k,\ell} |\phi_{k,\ell}\rangle\langle\phi_{k,\ell}|. \quad (3.4)$$

The completeness relations $\sum_k K_k^{U\dagger} K_k^U = \sum_\ell K_\ell^{V\dagger} K_\ell^V = \mathbf{I}$ guarantee that $\sum_{k,\ell} p_{k,\ell} = 1$.

3.3. Noisy probabilities. For measurement outcome $m \in \{0, 1, 2, 3\}$, we denote Π_m the projector onto the subspace $\{m, 4+m, \dots, 4(n-1)+m\}$.

Proposition 3.4. *Under general Kraus noise, the quantum measurement probability reads*

$$\tilde{\mathbb{P}}_m = \text{Tr}[\Pi_m \tilde{\rho}_2] = \sum_{k,\ell} p_{k,\ell} \sum_{j=0}^{n-1} |\langle 4j+m|\phi_{k,\ell}\rangle|^2, \quad \text{for each } m \in \{0, 1, 2, 3\}.$$

Proof. The first equality follows from the Born rule applied to (3.3). Using (3.4),

$$\begin{aligned} \text{Tr}[\Pi_m \tilde{\rho}_2] &= \sum_{k,\ell} p_{k,\ell} \text{Tr}[\Pi_m |\phi_{k,\ell}\rangle\langle\phi_{k,\ell}|] = \sum_{k,\ell} p_{k,\ell} \langle\phi_{k,\ell}|\Pi_m|\phi_{k,\ell}\rangle \\ &= \sum_{k,\ell} p_{k,\ell} \sum_{j=0}^{n-1} |\langle 4j+m|\phi_{k,\ell}\rangle|^2. \end{aligned}$$

□

Remark 3.5. Consider Kraus factors of the form

$$K_\ell^V = \sum_{\mathbf{g} \in \{\mathbf{I}, \mathbf{X}, \mathbf{Y}, \mathbf{Z}\}} v_\ell^{\mathbf{g}} \mathbf{G} \quad \text{and} \quad K_k^U = \sum_{\mathbf{g} \in \{\mathbf{I}, \mathbf{X}, \mathbf{Y}, \mathbf{Z}\}} u_k^{\mathbf{g}} \mathbf{G},$$

for some complex coefficients $(v_\ell^{\mathbf{g}})_\ell, (u_k^{\mathbf{g}})_k$. We actually assume that the operation of V is noiseless (which is not so demanding as V only consists of Hadamard gates), so that in fact

$K_\ell^V = \mathbf{I}$. Recall that $|\phi_{k,\ell}\rangle = \frac{1}{\sqrt{np_{k,\ell}}} \sum_{i=0}^{n-1} K_k^U \mathbf{U}(\boldsymbol{\theta}, \mathbf{x}) K_\ell^V |4i\rangle$. We can then write, for each $m \in \{0, 1, 2, 3\}$,

$$\begin{aligned}
 |\langle 4j + m | \phi_{k,\ell} \rangle|^2 &= \frac{1}{np_{k,\ell}} \left| \langle 4j + m | \sum_{i=0}^{n-1} K_k^U \mathbf{U}(\boldsymbol{\theta}, \mathbf{x}) K_\ell^V |4i\rangle \right|^2 \\
 &= \frac{1}{np_{k,\ell}} \left| \langle 4j + m | K_k^U \mathbf{U}(\boldsymbol{\theta}, \mathbf{x}) \sum_{i=0}^{n-1} |4i\rangle \right|^2 \\
 &= \frac{1}{np_{k,\ell}} \left| \langle 4j + m | K_k^U \mathbf{U}(\boldsymbol{\theta}, \mathbf{x}) \sum_{i=0}^{n-1} |4i\rangle \right|^2 \\
 &= \frac{1}{np_{k,\ell}} \left| \langle 4j + m | K_k^U \sum_{o=0}^3 \sum_{i=0}^{n-1} \alpha_{o,i} |4i + o\rangle \right|^2 \\
 &= \frac{1}{np_{k,\ell}} \left| \langle 4j + m | \sum_{o=0}^3 \sum_{i=0}^{n-1} \tilde{u}_{k,o,i} |4i + o\rangle \right|^2 \\
 &= \frac{1}{np_{k,\ell}} \left| \sum_{o=0}^3 \sum_{i=0}^{n-1} \tilde{u}_{k,o,i} \langle 4j + m | |4i + o\rangle \right|^2 \\
 &= \frac{|\tilde{u}_{k,m,j}|^2}{np_{k,\ell}},
 \end{aligned}$$

where we used the form of $\mathbf{U}(\boldsymbol{\theta}, \mathbf{x}) \sum_{i=0}^{n-1} |4i\rangle = \sum_{o=0}^3 \sum_{i=0}^{n-1} \alpha_{o,i} |4i + o\rangle$ for some coefficients $\alpha_{o,i}$, derived in the proof of [9, Proposition VI.1]. Regarding the actions of the K_k^U operators above, we have

$$K_k^U \sum_{o=0}^3 \sum_{i=0}^{n-1} \alpha_{o,i} |4i + o\rangle = \sum_{\mathbf{g} \in \{\mathbf{I}, \mathbf{X}, \mathbf{Y}, \mathbf{Z}\}} u_k^{\mathbf{g}} \mathbf{G} \left(\sum_{o=0}^3 \sum_{i=0}^{n-1} \alpha_{o,i} |4i + o\rangle \right) = \sum_{o=0}^3 \sum_{i=0}^{n-1} \tilde{u}_{k,o,i} |4i + o\rangle,$$

where the coefficients $\tilde{u}_{k,o,i}$ take into account $u_k^{\mathbf{g}}$ and $\alpha_{o,i}$. The final quantum measurement probabilities therefore read, for each $m \in \{0, 1, 2, 3\}$,

$$\tilde{\mathbb{P}}_m = \sum_k p_{k,\ell} \sum_{j=0}^{n-1} |\langle 4j + m | \phi_k \rangle|^2 = \frac{1}{n} \sum_k \sum_{j=0}^{n-1} |\tilde{u}_{k,m,j}|^2$$

3.4. Noisy Quantitative Universal Approximation Theorem. This section connects the noisy quantum neural network output to the quantitative Universal Approximation Theorem from [9]. We refer to Section 2 and (2.1) for the necessary tools. Similarly to using $\tilde{\cdot}$ for the noisy density operator (3.2), we keep this notation for the noisy version of the QNN output.

Theorem 3.6. *For any $R > 0$, $f \in \mathcal{F}_R$, $n \in \mathbb{N}$ and CPTP noise channels Ψ_V and Ψ_U , there exists $\boldsymbol{\theta} \in \Theta$ such that*

$$\left(\int_{\mathbb{R}^d} |f(\mathbf{x}) - \tilde{f}_{n,\boldsymbol{\theta}}^R(\mathbf{x})|^2 \mu(d\mathbf{x}) \right)^{1/2} \leq \frac{L^1[\hat{f}]}{\sqrt{n}} + 4R\sqrt{1 - \mathcal{F}_{\min}^2},$$

with $\tilde{f}_{n,\theta}^R(\cdot) = R \left[1 - 2 \left(\tilde{\mathbb{P}}_1 + \tilde{\mathbb{P}}_2 \right) \right]$ – mimicking (2.2) – and \mathcal{F}_{\min} is the worst-case fidelity

$$\mathcal{F}_{\min} := \inf_{k,\ell:p_{k,\ell}>0} \inf_{\boldsymbol{\theta} \in \Theta, \mathbf{x} \in \mathbb{R}^d} \left| \mathbf{V}^\dagger \mathbf{U}(\boldsymbol{\theta}, \mathbf{x})^\dagger \langle 0^{\otimes n} | \phi_{k,\ell} \rangle \right|.$$

Proof. By the triangle inequality, we can decompose the error as

$$\left\| f - \tilde{f}_{n,\theta}^R \right\|_{L^2(\mu)} \leq \left\| f - f_{n,\theta}^R \right\|_{L^2(\mu)} + \left\| f_{n,\theta}^R - \tilde{f}_{n,\theta}^R \right\|_{L^2(\mu)}.$$

For the first term, the quantitative quantum Universal Approximation Theorem [9, Theorem II.4] yields that there exists $\boldsymbol{\theta} \in \Theta$ such that

$$\left\| f - f_{n,\theta}^R \right\|_{L^2(\mu)} \leq \frac{L^1[\hat{f}]}{\sqrt{n}}.$$

For the noise-induced part, the output is

$$\tilde{f}_{n,\theta}^R(\cdot) = R \left[1 - 2 \left(\tilde{\mathbb{P}}_1 + \tilde{\mathbb{P}}_2 \right) \right],$$

so that Proposition 3.4 gives

$$\begin{aligned} \left| f_{n,\theta}^R(\mathbf{x}) - \tilde{f}_{n,\theta}^R(\mathbf{x}) \right| &= 2R \left| \left(\mathbb{P}_1 + \mathbb{P}_2 \right) - \left(\tilde{\mathbb{P}}_1 + \tilde{\mathbb{P}}_2 \right) \right| \\ &= 2R \left| \sum_{m=1,2} \left[\text{Tr}[\Pi_m \rho_2] - \sum_{k,\ell} p_{k,\ell} |\langle \phi_{k,\ell} | \Pi_m \langle \phi_{k,\ell} \rangle| \right] \right|. \end{aligned} \quad (3.5)$$

To bound (3.5), we average over the trajectories of the Kraus operators. For that purpose, let $\mathcal{F}_{k,\ell}(\boldsymbol{\theta}, \mathbf{x}) := |\langle \psi_2(\boldsymbol{\theta}, \mathbf{x}) | \phi_{k,\ell} \rangle|$ denote the trajectory fidelity where $|\psi_2(\boldsymbol{\theta}, \mathbf{x})\rangle = \mathbf{U}(\boldsymbol{\theta}, \mathbf{x}) \mathbf{V} | 0 \rangle^{\otimes n}$ is the noiseless evolved state. Recall that the worst-case fidelity is

$$\mathcal{F}_{\min} := \inf_{k,\ell:p_{k,\ell}>0} \inf_{\boldsymbol{\theta} \in \Theta, \mathbf{x} \in \mathbb{R}^d} \mathcal{F}_{k,\ell}(\boldsymbol{\theta}, \mathbf{x}).$$

Secondly, for each trajectory, the deviation in measurement probability satisfies

$$\left| \text{Tr} \left[\Pi_m |\psi_2(\boldsymbol{\theta}, \mathbf{x})\rangle \langle \psi_2(\boldsymbol{\theta}, \mathbf{x})| \right] - \text{Tr} \left[\Pi_m |\phi_{k,\ell}\rangle \langle \phi_{k,\ell}| \right] \right| \leq \sqrt{1 - \mathcal{F}_{k,\ell}^2}$$

by the Fuchs-van de Graaf inequality [24, Section 9.2.3]. Thus (3.5) can be bounded as

$$\begin{aligned} \left\| f_{n,\theta}^R - \tilde{f}_{n,\theta}^R \right\|_{L^2(\mu)} &\leq 2R \sum_{m=1,2} \left\| \sum_{k,\ell} p_{k,\ell} [\langle \psi_2(\boldsymbol{\theta}, \mathbf{x}) | \Pi_m | \psi_2(\boldsymbol{\theta}, \mathbf{x}) \rangle - \langle \phi_{k,\ell} | \Pi_m | \phi_{k,\ell} \rangle] \right\|_{L^2(\mu)} \\ &\leq 4R \sqrt{1 - \mathcal{F}_{\min}^2}. \end{aligned}$$

□

Remark 3.7. During physical training, the parameters $\boldsymbol{\theta}$ are optimised with respect to noisy measurement outcomes $\tilde{\mathbb{P}}_m$. This means the learnt function $\tilde{f}_{n,\theta}^R$ directly approximates the target f , and not an intermediate ideal function.

3.5. Depolarising noise channel. The depolarising channel is one of the very common quantum channels used to model quantum noise [24, Section 8.3.4].

Definition 3.8. The \mathfrak{d} -dimensional depolarising channel is the CPTP map

$$\Delta_\lambda(\rho) = (1 - \lambda)\rho + \frac{\lambda}{\mathfrak{d}}\mathbf{I},$$

where $\mathfrak{d} = 2^n$ is the Hilbert space dimension, n the number of qubits, and the constraint $\lambda \in [0, 1 + \frac{1}{\mathfrak{d}^2 - 1}]$ ensures complete positivity. For an orthogonal basis of unitary operators $\{\mathbf{U}_i\}_{i=0}^{\mathfrak{d}^2 - 1}$ such that $\mathbf{U}_0 = \mathbf{I}$ and $\text{Tr}[\mathbf{U}_i^\dagger \mathbf{U}_j] = \mathfrak{d}\delta_{ij}$, the general Kraus decomposition reads

$$K_0 = \sqrt{1 - \lambda \frac{\mathfrak{d}^2 - 1}{\mathfrak{d}^2}}\mathbf{I}, \quad K_i = \sqrt{\frac{\lambda}{\mathfrak{d}^2}}\mathbf{U}_i \quad \text{for } i \in \{1, \dots, \mathfrak{d}^2 - 1\}.$$

In particular, in the $n = 1$ -qubit case, taking the Pauli $\{\mathbf{I}, \mathbf{X}, \mathbf{Y}, \mathbf{Z}\}$, we have

$$K_0 = \sqrt{1 - \frac{3\lambda}{4}}\mathbf{I}, \quad K_1 = \sqrt{\frac{\lambda}{2}}\mathbf{X}, \quad K_2 = \sqrt{\frac{\lambda}{2}}\mathbf{Y}, \quad K_3 = \sqrt{\frac{\lambda}{2}}\mathbf{Z}.$$

Proposition 3.9. Under depolarising noise Δ_λ , the noisy state (3.2) reads

$$\tilde{\rho}_2^\Delta = (1 - \lambda_V)(1 - \lambda_U)\rho_2 + [(1 - \lambda_U)\lambda_V + \lambda_U] \frac{\mathbf{I}}{2^n}. \quad (3.6)$$

Proof. Clearly, from [9], both \mathbf{V} and \mathbf{U} are unitary, so that $\mathbf{U}\mathbf{U}^\dagger = \mathbf{V}\mathbf{V}^\dagger = \mathbf{I}$. Applying depolarising noise after each gate, we obtain

$$\begin{aligned} \tilde{\rho}_2^\Delta &= \Delta_{\lambda_U}(\mathbf{U}(\boldsymbol{\theta}, \mathbf{x})\Delta_{\lambda_V}(\rho_1)\mathbf{U}^\dagger(\boldsymbol{\theta}, \mathbf{x})) = \Delta_{\lambda_U}\left((1 - \lambda_V)\rho_2 + \frac{\lambda_V}{2^n}\mathbf{I}\right) \\ &= (1 - \lambda_V)(1 - \lambda_U)\rho_2 + [(1 - \lambda_U)\lambda_V + \lambda_U] \frac{\mathbf{I}}{2^n}. \end{aligned}$$

□

The proposition provides us with an explanation about how noise affects the original state. This then allows us to precisely quantify the error induced by the depolarisation. A common metric in quantum computing to evaluate this is the following [24, Section 9.2.2]:

Definition 3.10. The *fidelity* between two density operators ρ and σ reads

$$\mathcal{F}[\rho, \sigma] := \text{Tr} \left[\sqrt{\rho^{\frac{1}{2}} \sigma \rho^{\frac{1}{2}}} \right].$$

In particular, given a pure quantum state $|\psi\rangle$ and some density operator σ , we can write

$$\mathcal{F}[|\psi\rangle\langle\psi|, \sigma] = \text{Tr} \left[\left(\sqrt{|\psi\rangle\langle\psi|} \sigma \sqrt{|\psi\rangle\langle\psi|} \right)^{\frac{1}{2}} \right] = \text{Tr} \left[(|\psi\rangle\langle\psi| \sigma)^{\frac{1}{2}} \right] = \text{Tr} \left[\sqrt{\langle\psi|\sigma|\psi\rangle} \right] = \sqrt{\langle\psi|\sigma|\psi\rangle}.$$

Consider for example (3.6) and the noiseless version $\rho_2 = \mathbf{U}(\boldsymbol{\theta}, \mathbf{x})\mathbf{V}\rho_0\mathbf{V}^\dagger\mathbf{U}^\dagger(\boldsymbol{\theta}, \mathbf{x})$ in (3.1).

Proposition 3.11. Let $\rho_0 = |0\rangle\langle 0|$ (so that ρ_2 is the density operator corresponding to the pure state $|\psi_2(\boldsymbol{\theta}, \mathbf{x})\rangle = \mathbf{U}(\boldsymbol{\theta}, \mathbf{x})\mathbf{V}|0\rangle$). Then, the fidelity for $\tilde{\rho}_2^\Delta$ is

$$\mathcal{F}[\rho_2, \tilde{\rho}_2^\Delta] = \left((1 - \lambda_V)(1 - \lambda_U) + \frac{[(1 - \lambda_U)\lambda_V + \lambda_U]}{2^n} \right)^{\frac{1}{2}}.$$

Proof.

$$\begin{aligned}
\mathcal{F}[\rho_2, \tilde{\rho}_2^\Delta]^2 &= \langle \psi_2(\boldsymbol{\theta}, \mathbf{x}) | \tilde{\rho}_2^\Delta | \psi_2(\boldsymbol{\theta}, \mathbf{x}) \rangle \\
&= \langle 0 | \mathbf{V}^\dagger \mathbf{U}^\dagger(\boldsymbol{\theta}, \mathbf{x}) \tilde{\rho}_2^\Delta \mathbf{U}(\boldsymbol{\theta}, \mathbf{x}) \mathbf{V} | 0 \rangle \\
&= \langle 0 | \mathbf{V}^\dagger \mathbf{U}^\dagger(\boldsymbol{\theta}, \mathbf{x}) \left((1 - \lambda_{\mathbf{V}})(1 - \lambda_{\mathbf{U}})\rho_2 + [(1 - \lambda_{\mathbf{U}})\lambda_{\mathbf{V}} + \lambda_{\mathbf{U}}] \frac{\mathbf{I}}{2^n} \right) \mathbf{U}(\boldsymbol{\theta}, \mathbf{x}) \mathbf{V} | 0 \rangle \\
&= (1 - \lambda_{\mathbf{V}})(1 - \lambda_{\mathbf{U}}) \langle 0 | \mathbf{V}^\dagger \mathbf{U}^\dagger(\boldsymbol{\theta}, \mathbf{x}) \rho_2 \mathbf{U}(\boldsymbol{\theta}, \mathbf{x}) \mathbf{V} | 0 \rangle \\
&\quad + \frac{[(1 - \lambda_{\mathbf{U}})\lambda_{\mathbf{V}} + \lambda_{\mathbf{U}}]}{2^n} \langle 0 | \mathbf{V}^\dagger \mathbf{U}^\dagger(\boldsymbol{\theta}, \mathbf{x}) \mathbf{U}(\boldsymbol{\theta}, \mathbf{x}) \mathbf{V} | 0 \rangle \\
&= (1 - \lambda_{\mathbf{V}})(1 - \lambda_{\mathbf{U}}) + \frac{[(1 - \lambda_{\mathbf{U}})\lambda_{\mathbf{V}} + \lambda_{\mathbf{U}}]}{2^n}.
\end{aligned}$$

□

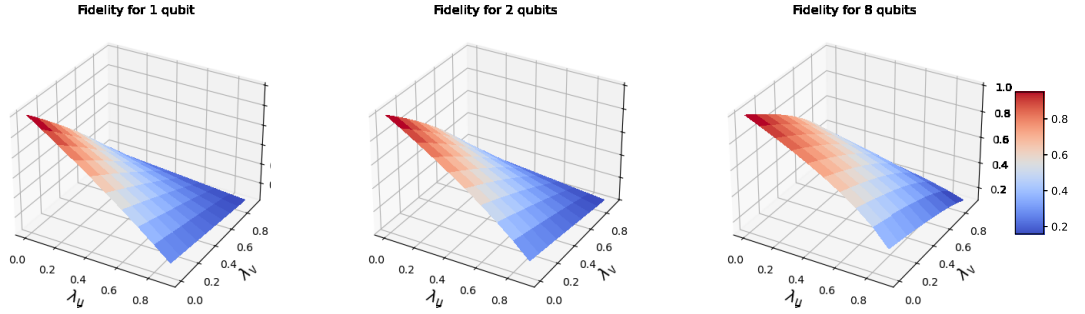


FIGURE 1. Fidelity computed in Proposition 3.11 with $\mathbf{n} \in \{1, 2, 8\}$ qubits.

Proposition 3.12. *The probability of outcome $m \in \{0, 1, 2, 3\}$ reads*

$$\tilde{\mathbb{P}}_m = \alpha \mathbb{P}_m + (1 - \alpha) \frac{n}{2^n}, \quad \text{where } \alpha := (1 - \lambda_{\mathbf{V}})(1 - \lambda_{\mathbf{U}}), \quad (3.7)$$

where \mathbb{P}_m is the noiseless probability and where we recall that $\mathbf{n} = \lceil \log_2(4n + n_0) \rceil$.

Proof. From Proposition 3.4 and Proposition 3.9, we can write, for each $m \in \{0, 1, 2, 3\}$,

$$\begin{aligned}
\tilde{\mathbb{P}}_m &= \text{Tr} \left[\Pi_m \tilde{\rho}_2 \right] = \text{Tr} \left[\Pi_m \left((1 - \lambda_{\mathbf{V}})(1 - \lambda_{\mathbf{U}})\rho_2 + [(1 - \lambda_{\mathbf{U}})\lambda_{\mathbf{V}} + \lambda_{\mathbf{U}}] \frac{\mathbf{I}}{2^n} \right) \right] \\
&= (1 - \lambda_{\mathbf{V}})(1 - \lambda_{\mathbf{U}}) \text{Tr}[\Pi_m \rho_2] + [(1 - \lambda_{\mathbf{U}})\lambda_{\mathbf{V}} + \lambda_{\mathbf{U}}] \text{Tr} \left[\Pi_m \frac{\mathbf{I}}{2^n} \right] \\
&= (1 - \lambda_{\mathbf{V}})(1 - \lambda_{\mathbf{U}}) \mathbb{P}_m + \frac{1}{2^n} [(1 - \lambda_{\mathbf{U}})\lambda_{\mathbf{V}} + \lambda_{\mathbf{U}}] \text{Tr}[\Pi_m].
\end{aligned}$$

The proposition then follows once we show that $\text{Tr}[\Pi_m] = n$. Let \mathcal{K}_m be the target set of measurement outcomes defined as $\mathcal{K}_m := \{m, 4 + m, \dots, 4(n - 1) + m\}$. The projection operator Π_m onto the subset of orthonormal computational basis states defined by \mathcal{K}_m can be written explicitly as

$$\Pi_m = \sum_{k \in \mathcal{K}_m} |k\rangle \langle k| = \sum_{i=0}^{n-1} |4i + m\rangle \langle 4i + m|.$$

The trace of an operator is independent of the basis chosen. In the computational basis of the Hilbert space, denoted $\{|j\rangle\}_{j=0}^{N-1}$, it reads

$$\begin{aligned} \text{Tr}[\Pi_m] &= \sum_{j=0}^{N-1} \langle j | \Pi_m | j \rangle = \sum_{j=0}^{N-1} \langle j | \left(\sum_{i=0}^{n-1} |4i+m\rangle \langle 4i+m| \right) | j \rangle \\ &= \sum_{i=0}^{n-1} \sum_{j=0}^{N-1} \langle j | 4i+m \rangle \langle 4i+m | j \rangle = \sum_{i=0}^{n-1} \sum_{j=0}^{N-1} |\langle j | 4i+m \rangle|^2 = n. \end{aligned}$$

□

In this depolarising setting, the output function of the quantum neural network, as introduced in Theorem 3.6, takes the following explicit form:

Corollary 3.13. *The QNN output under the depolarising noise reads*

$$\tilde{f}_{n,\theta}^R(\mathbf{x}) = \alpha f_{n,\theta}^R(\mathbf{x}) + R(1-\alpha) \left(1 - \frac{4n}{2^n} \right),$$

with $f_{n,\theta}^R(\cdot)$ the ideal QNN output from (2.2).

Remark 3.14. A useful simplification occurs when $n_0 = 0$, namely when choosing n and \mathbf{n} as $2^n = 4n$. In this case, Corollary 3.13 reduces to $\tilde{f}_{n,\theta}^R(\mathbf{x}) = \alpha f_{n,\theta}^R(\mathbf{x})$, with α in (3.7).

Proof. By definition,

$$\begin{aligned} \tilde{f}_{n,\theta}^R(\mathbf{x}) &= R - 2R \left(\tilde{\mathbb{P}}_1 + \tilde{\mathbb{P}}_2 \right) \\ &= R - 2R \left[\alpha(\mathbb{P}_1 + \mathbb{P}_2) + 2(1-\alpha) \frac{n}{2^n} \right] \\ &= R - 2R\alpha(\mathbb{P}_1 + \mathbb{P}_2) - 4R(1-\alpha) \frac{n}{2^n} \\ &= R - 2R\alpha \frac{R - f_{n,\theta}^R(\mathbf{x})}{2R} - 4R(1-\alpha) \frac{n}{2^n}, \end{aligned}$$

using the definition of $f_{n,\theta}^R(\cdot)$ in (2.2) and the corollary follows. □

In the next corollary, we show that by adding an additional regression layer to the QNN, we are able to cancel out the noise. Thereby we can address the noise by building a hardware-specific algorithm to recover the noiseless circuit.

Corollary 3.15. *Consider the QNN $\tilde{f}_{n,\bar{\theta}}^R(\cdot)$ built from the noisy QNN $\tilde{f}_{n,\theta}^R(\cdot)$ by adding two trainable parameters $\beta_1, \beta_2 \in \mathbb{R}$:*

$$\tilde{f}_{n,\bar{\theta}}^R(\mathbf{x}) = \beta_1 \tilde{f}_{n,\theta}^R(\mathbf{x}) + \beta_2,$$

where we denote $\bar{\theta} = (\theta, \beta_1, \beta_2)$. Then, there exist β_1, β_2 such that

$$\tilde{f}_{n,\bar{\theta}}^R(\mathbf{x}) = f_{n,\theta}^R(\mathbf{x}),$$

that is, by optimal QNN-training one can offset the noise and recover the ideal QNN output.

In the particular case of Remark 3.14, one only needs to train β_1 since β_2 is null.

Proof. Select $\beta_1 = \frac{1}{\alpha}$ and $\beta_2 = -\beta_1 R(1 - \alpha) \left(1 - \frac{4n}{2^n}\right)$. Then, Corollary 3.13 shows that

$$\tilde{f}_{n,\bar{\theta}}^R(\mathbf{x}) = \beta_1 \tilde{f}_{n,\theta}^R(\mathbf{x}) + \beta_2 = \beta_1 \alpha f_{n,\theta}^R(\mathbf{x}) + \beta_1 R(1 - \alpha) \left(1 - \frac{4n}{2^n}\right) + \beta_2 = f_{n,\theta}^R(\mathbf{x}).$$

□

We can now provide an accurate bound for the QNN in the depolarising case:

Theorem 3.16 (Universal approximation with depolarising noise). *For any $R > 0$, $f \in \mathcal{F}_R$, $n \in \mathbb{N}$, and depolarising noise parameters (λ_V, λ_U) , there exists $\theta \in \Theta$ such that*

$$\left| \int_{\mathbb{R}^d} \left| f(\mathbf{x}) - \tilde{f}_{n,\theta}^R(\mathbf{x}) \right|^2 \mu(dx) \right|^{\frac{1}{2}} \leq \frac{\alpha L^1[\hat{f}]}{\sqrt{n}} + (1 - \alpha) \|f\|_{L^2(\mu)} + R(1 - \alpha) \left(1 - \frac{4n}{2^n}\right). \quad (3.8)$$

Note that the last term disappears in the particular case of Remark 3.14.

Proof. From Corollary 3.13 and the triangle inequality,

$$\begin{aligned} \|f - \tilde{f}_{n,\theta}^R\|_{L^2(\mu)} &= \left\| f - \alpha f_{n,\theta}^R - R(1 - \alpha) + 4R(1 - \alpha) \frac{n}{2^n} \right\|_{L^2(\mu)} \\ &\leq \left\| f - \alpha f_{n,\theta}^R \right\|_{L^2(\mu)} + \left| R(1 - \alpha) - 4R(1 - \alpha) \frac{n}{2^n} \right| \|\mathbf{1}\|_{L^2(\mu)} \\ &= \|f - \alpha f_{n,\theta}^R\|_{L^2(\mu)} + R(1 - \alpha) \left(1 - \frac{4n}{2^n}\right), \end{aligned}$$

where $\|\mathbf{1}\|_{L^2(\mu)} = 1$ since μ is a probability measure. Bound the deviation from the scaled ideal output can be done by adding and subtracting αf and using the triangle inequality:

$$\begin{aligned} \|f - \alpha f_{n,\theta}^R\|_{L^2(\mu)} &\leq \|f - \alpha f\|_{L^2(\mu)} + \left\| \alpha f - \alpha f_{n,\theta}^R \right\|_{L^2(\mu)} \\ &= \|f - \alpha f\|_{L^2(\mu)} + \alpha \left\| f - f_{n,\theta}^R \right\|_{L^2(\mu)} \\ &= (1 - \alpha) \|f\|_{L^2(\mu)} + \alpha \left\| f - f_{n,\theta}^R \right\|_{L^2(\mu)}. \end{aligned}$$

The last term can be identified as the object of the original noiseless Universal Approximation Theorem and bounded as $\|f - f_{n,\theta}^R\|_{L^2(\mu)} \leq \frac{L^1[\hat{f}]}{\sqrt{n}}$, therefore (3.8) follows from

$$\left\| f - \alpha f_{n,\theta}^R \right\|_{L^2(\mu)} \leq (1 - \alpha) \|f\|_{L^2(\mu)} + \frac{\alpha L^1[\hat{f}]}{\sqrt{n}}.$$

□

Remark 3.17. The total approximation error has three contributions:

- (1) *Statistical:* $\frac{\alpha L^1[\hat{f}]}{\sqrt{n}}$ is the bound from [9] scaled by the hardware fidelity factor α . As noise increases (α decreases), this term worsens.
- (2) *Systematic:* $(1 - \alpha) \|f\|_{L^2(\mu)}$ represents the fundamental limitation: noisy circuits cannot perfectly reproduce the target function. As α approaches 1 (low noise), this vanishes.
- (3) *Offset:* the term $R(1 - \alpha) \left(1 - \frac{4n}{2^n}\right)$ is a constant shift introduced by the maximally mixed component of the noise and depends on the qubit count.

3.6. Hardware-parameterised model for depolarising noise. The parameters λ_V and λ_U are *effective* depolarising parameters determined by the physical circuit implementation. They are not free parameters but are computed from gate counts and hardware error rates.

3.6.1. *Noisy V gate.* As shown in the appendix of [9], the V gate is simply built from

$$N_{1q} := n - 2$$

one-qubit Hadamard gates. For independent single-qubit depolarising noise with error rate ε_{1q} per (Hadamard) gate, the effective parameter is thus

$$\lambda_v = 1 - (1 - \varepsilon_{1q})^{n-2}.$$

3.6.2. *Noisy U gate.* The naive multi-controlled implementation of U requires $N_{2q} = n^2$ two-qubit gates, but its implementation via Uniformly Controlled Rotations reduces this by a factor of roughly 15 (though it varies from application to application), so we set

$$N_{2q} \approx \frac{n^2}{15} = \frac{n \cdot \lceil \log_2(4n + n_0) \rceil}{15},$$

For a two-qubit gate error rate ε_{2q} , the effective parameter from gate errors alone is

$$\lambda_u = 1 - (1 - \varepsilon_{2q})^{N_{2q}}.$$

3.6.3. *Decoherence Contributions.* The circuit execution time $t_{\text{circ}} := \max\{N_{2q}t_{2q}, N_{1q}t_{1q}\}$, where t_{1q} and t_{2q} denote respectively the execution time of one-qubit and two-qubit gates, leads to additional decoherence. For relaxation time T_1 (amplitude damping) and dephasing time T_2 (phase damping), the error probabilities are

$$p_{T_1} = 1 - \exp\left\{-\frac{t_{\text{circ}}}{T_1}\right\}, \quad p_{T_2} = 1 - \exp\left\{-\frac{t_{\text{circ}}}{T_2}\right\}.$$

The combined effective λ_u including decoherence is approximately

$$\lambda_u \approx 1 - (1 - \lambda_u) \left(1 - \frac{1}{2}p_{T_1}\right) \left(1 - \frac{1}{2}p_{T_2}\right).$$

3.6.4. *Combined characterisation.* We introduce the depolarised hardware parameters

$$\varepsilon := (\varepsilon_{1q}, \varepsilon_{2q}, T_1, T_2, t_{2q}, N_{2q}).$$

Table 1 summarises the noise parameters for the IBM quantum backend `ibm_vez` (Heron r2 processor), Quantinuum H2, and the latest Rigetti modular system (Cepheus-1-36Q).

Hardware	Parameter	Symbol	Value	Source
IBM <code>ibm_fez</code>	Single-qubit gate error (\sqrt{X})	ε_{1q}	$2.761 \cdot 10^{-4}$	Live calibration [13]
	Two-qubit gate error (cZ)	ε_{2q}	$2.548 \cdot 10^{-3}$	Live calibration [13]
	Relaxation time	T_1	$144.97 \mu s$	Live calibration [13]
	Dephasing time	T_2	$99.9 \mu s$	Live calibration [13]
	Two-qubit gate duration	t_{2q}	68 ns	Hardware spec. [1]
	Circuit execution time (per N_{2q})	t_{circ}	$68N_{2q}$ ns	Computed
	p_{T_1}	p_{T_1}	$1 - \exp\{-t_{\text{circ}}/T_1\}$	Computed
	p_{T_2}	p_{T_2}	$1 - \exp\{-t_{\text{circ}}/T_2\}$	Computed
	λ_U	$1 - (1 - \varepsilon_{2q})^{N_{2q}}$	Computed	
Quantinuum H2	Single-qubit gate infidelity	ε_{1q}	$3 \cdot 10^{-5}$	Datasheet [27]
	Two-qubit gate infidelity	ε_{2q}	$1 \cdot 10^{-3}$	Datasheet [27]
	Single-qubit gate duration	t_{1q}	$\sim 5 \mu s$	Datasheet [27]
	Two-qubit gate duration	t_{2q}	$\sim 100 \mu s$	Datasheet [27]
	Memory error per qubit (depth-1)	λ_{mem}	$2 \cdot 10^{-4}$	Datasheet [27]
	State prep/meas error	r	$1 \cdot 10^{-3}$	Datasheet [27]
Rigetti Cepheus	Two-qubit gate error	ε_{2q}	$5 \cdot 10^{-3}$	Press release [31]
	Gate speed	t_{2q}	60–80 ns	Technical specs [30]
	T_1 (typical superconducting)	T_1	$\sim 50\text{--}100 \mu s$	Technical specs [31]
	T_2 (typical superconducting)	T_2	$\sim 20\text{--}50 \mu s$	Technical specs [31]

TABLE 1. Hardware parameters and computed depolarising noise parameters for IBM `ibm_fez` (Heron r2, 156 qubits), Quantinuum H2 (56 qubits, trapped-ion), and Rigetti Cepheus-1-36Q (36 qubits, modular superconducting). Raw hardware parameters are sourced from live calibration or official datasheets; computed parameters (λ_V , λ_U , λ_V , and decoherence terms) are taken from Section 3.6. IBM values current as of January 2026; Quantinuum values from official product datasheet; Rigetti values from July 2025 announcement with August 2025 deployment.

3.7. Readout error in the depolarising case. Readout error is a classical effect occurring after wavefunction collapse and must be modelled separately from quantum noise.

Definition 3.18. Let \mathbf{p} denote the single-qubit readout error probability (probability of a bit-flip during measurement). For measurement outcome $m \in \{0, 1, 2, 3\}$ encoded in the two target qubits, the measured probability reads

$$\bar{\mathbb{P}}_m := \sum_{m'=0}^3 q_{m,m'} \tilde{\mathbb{P}}_{m'}$$

with $\tilde{\mathbb{P}}_{m'}$ the probability of output m' in the noisy neural above; the confusion matrix $Q = (q_{m,m'})$ gives the probabilities of measuring outcome m when the true quantum state would yield m' : $q_{m,m'} = \mathbf{p}^{H(m,m')}(1-\mathbf{p})^{2-H(m,m')}$, with $H(m,m')$ the Hamming distance between the 2-bit binary representations of m and m' .

Proposition 3.19. *For depolarising noise with readout error \mathbf{p} , the approximation bound is, with $\bar{f}_{n,\theta}^R := R\{1 - 2(\bar{\mathbb{P}}_1 + \bar{\mathbb{P}}_2)\}$,*

$$\left| \int_{\mathbb{R}^d} \left| f(\mathbf{x}) - \bar{f}_{n,\theta}^R(\mathbf{x}) \right|^2 \mu(d\mathbf{x}) \right|^{\frac{1}{2}} \leq \frac{\alpha}{\sqrt{n}} L^1[\hat{f}] + (1-\alpha) \|f\|_{L^2(\mu)} + R(1-\alpha) \left(1 - \frac{4n}{2^n}\right) + 4R\mathbf{p}.$$

Proof. The matrix Q yields the perturbation $\bar{\mathbb{P}}_m - \tilde{\mathbb{P}}_m = \sum_{m' \neq m} q_{m,m'} \tilde{\mathbb{P}}_{m'} - \sum_{m' \neq m} q_{m',m} \tilde{\mathbb{P}}_{m'}$. For the QNN output, $\left| \bar{f}_{n,\theta}^R(\mathbf{x}) - \tilde{f}_{n,\theta}^R(\mathbf{x}) \right| = 2R \left| \sum_{m=1,2} (\bar{\mathbb{P}}_m - \tilde{\mathbb{P}}_m) \right|$. In the worst case when all probability mass migrates to wrong outcomes, $\max_{m,m'} |\bar{\mathbb{P}}_m - \tilde{\mathbb{P}}_m| \leq 2\mathbf{p}$, since at most two bit flips can occur. Therefore, $\|\bar{f}_{n,\theta}^R - \tilde{f}_{n,\theta}^R\|_{L^2(\mu)} \leq 4R\mathbf{p}$. Combining with (3.8) via triangle inequality gives the theorem. \square

4. NUMERICAL EXPERIMENTS

This section provides details regarding the implementation and the specificities of the quantum circuit. We consider the Black-Scholes model as in Section 2.3.3. These numerical experiments are designed to validate the non-asymptotic theoretical bounds within the finite-qubit regime and to assess the practical viability of the network under realistic hardware constraints. The findings confirm that the empirical approximation errors consistently respect the derived theoretical limits, demonstrating that the architecture models expectation functions even under noise on physical quantum processors.

4.1. Circuit architecture details.

Input Normalisation. The Black-Scholes parameters (S, K, T, r, σ) are normalised to the hypercube $[0, 1]^5$ via the affine transformation

$$x := \frac{x - \underline{x}}{\bar{x} - \underline{x}}, \quad \text{for } x \in \{S, K, T, r, \sigma\}, \text{ with } \underline{x} := \min x \text{ and } \bar{x} := \max x. \quad (4.1)$$

Any value outside the training range is clamped to $[0, 1]$ to prevent extrapolation artefacts. The scaling parameter R is set to $R = \lceil 1.1 \times \max_i P_i \rceil$, where P_i denotes the target option price at the i -th training point. This ensures all target prices lie within $[0, R]$.

Circuit architecture. For accuracy parameter n (the number of “accuracy blocks”), the circuit operates on $\mathbf{n} = \lceil \log_2(4n) \rceil$ qubits, and we consider here $n = 8$, or $\mathbf{n} = 5$ qubits. The circuit comprises three stages:

- (1) **State preparation (V):** Hadamard gates applied to the $(\mathbf{n} - 2)$ control qubits, leaving the two target qubits in $|00\rangle$.
- (2) **Parameterised unitary (U):** Block-diagonal unitary implementing n accuracy blocks, each contributing a term to the Fourier-like approximation.
- (3) **Measurement:** Computational basis measurement.

Uniformly Controlled Rotation Decomposition. The parameterised unitary $\mathbf{U}(\boldsymbol{\theta})$ introduced in [9] has block-diagonal structure

$$\mathbf{U}(\boldsymbol{\theta}, \mathbf{x}) = \sum_{k=0}^{n-1} |k\rangle\langle k| \otimes \bar{\mathbf{U}}^{(k)}(\boldsymbol{\theta}^k, \mathbf{x}),$$

with $\boldsymbol{\theta}^k = (\mathbf{a}^k, b^k, \gamma^k)$ and where each $\bar{\mathbf{U}}^{(k)}(\boldsymbol{\theta}^k, \mathbf{x}) = \mathbf{U}_1^{(k)}(\mathbf{a}^k, b^k, \mathbf{x}) \otimes \mathbf{U}_2^{(k)}(\gamma^k)$ acts on the two target qubits. A naive implementation using multi-controlled gates yields $\mathcal{O}(nn)$ two-qubit gates. However, *Uniformly controlled rotations* (UCR) (we refer the reader to [23], where these gates are introduced and detailed) allow the decomposition of \mathbf{U} into:

- One UCR_z on target qubit 0, conjugated by Hadamard gates;
- One UCR_y on target qubit 1.

This reduces the two-qubit gate count by a factor of about 15 compared to multi-controlled decomposition, critical for hardware execution where two-qubit gate errors dominate (in particular to keep λ_{U} small on hardware, as in Table 1).

Parameters optimisation. We implement three parameter optimisation strategies:

Method	Algorithm	Description
A	L-BFGS-B	Quasi-Newton with box constraints; simultaneous optimisation of all parameters
B	Two-stage	First optimise (\mathbf{a}, b) with fixed γ , then refine γ
C	Adam	Gradient descent with adaptive learning rates

For the loss function, we consider the usual mean-squared error

$$\mathcal{L}(\theta) := \frac{1}{2^n} \sum_{i=1}^{2^n} \left(f_n^R(x_i; \theta) - P_i \right)^2.$$

Measurement. Outcomes are grouped to extract the probabilities $\{\mathbb{P}_m\}_{m=0,\dots,3}$. For each outcome $o \in \{0, \dots, 2^n - 1\}$, we write $o = 4k + m$ with $k \in \{0, \dots, n - 1\}$, $m \in \{0, 1, 2, 3\}$. Only outcomes with $k < n$ contribute (states with $k \geq n$ arise from padding to a power-of-two dimension). The probability \mathbb{P}_m accumulates counts from all valid $o \equiv j \pmod{4}$:

$$\mathbb{P}_m = \frac{1}{N_{\text{shots}}} \sum_{\substack{o: o \bmod 4 = m \\ o < 4n}} c_o,$$

where c_o denotes the count for outcome o . The output of the quantum neural network is then computed as (see for example Corollary 3.13) $f_n^R(\mathbf{x}) = R[1 - 2(\mathbb{P}_1 + \mathbb{P}_2)]$.

Hardware execution. The circuits are run on `ibm_fez` using Qiskit Runtime’s `SamplerV2` primitive, which requires *Instruction Set Architecture* (ISA) circuits. Key steps included:

- **Transpilation:** Circuits are transpiled with `optimization_level=3`, mapping abstract gates to the backend’s native gate set and optimising for depth.
- **Batching:** All test circuits are submitted as a single job to minimise queue overhead.
- **Shot budget:** $N_{\text{shots}} = 8192$ per circuit, balancing statistical precision vs runtime.

The statistical error on the output price is

$$2R\sqrt{\frac{(\mathbb{P}_1 + \mathbb{P}_2)(1 - \mathbb{P}_1 - \mathbb{P}_2)}{N_{\text{shots}}}}. \quad (4.2)$$

Experiments are implemented in `Python-qiskit` and executed either on simulators (via `qiskit-aer`) or on the backend `ibm_fez`, with noise parameters $(\varepsilon_{1q}, \varepsilon_{2q}, \mathbf{p}, T_1, T_2)$ in Table 1.

4.1.1. *Circuit validation.* For each random parameter triple $(\boldsymbol{\theta}, \mathbf{x})$, the circuit’s sampled output is compared against the analytical formula

$$f_{n,\boldsymbol{\theta}}^R(\mathbf{x}) = \frac{1}{n} \sum_{i=1}^n R \cos(\gamma_i) \cos(\mathbf{b}_i + \mathbf{a}_i \cdot \mathbf{x})$$

derived in [9]. The residuals are uniformly bounded by $R/\sqrt{N_{\text{shots}}}$ across all tested configurations, confirming correct circuit implementation. The parameterised unitary \mathbf{U} is built using uniformly controlled rotations (UCR) [23]. The inner product $|\langle \psi_{\text{UCR}} | \psi_{\text{naive}} \rangle|$ equals 1 to tolerance 10^{-9} for all $n \in \{2, 4, 8\}$, $d \in \{1, 5\}$, and parameter scales $\in \{0.1, 1.0, 5.0\}$ (three random parameter sets each).

4.2. **Gaussian density approximation.** We first consider a simple version of Statement 2.1 and Proposition 2.2, in dimension $d = 1$, with L the random variable equal to zero almost surely, $\mu(\cdot)$ the Lebesgue measure, and \mathcal{N} the Gaussian density, as in Section 2.3.1. Then $\mathbb{E}[\mathcal{N}(e^{x+L})] = f_\sigma(x)$. The quantum neural network with n accuracy blocks then approximates f_σ with error $\varepsilon_n := \frac{L^1[\hat{f}_\sigma]}{\sqrt{n}} = \frac{1}{\sigma\sqrt{2\pi n}}$, hence, for a given approximation accuracy $\varepsilon > 0$, the required number of accuracy blocks is

$$n \geq \frac{1}{2\pi\sigma^2\varepsilon^2}. \quad (4.3)$$

Considering the case $n_0 = 0$, i.e. $4n = 2^n$, this can be recast in the minimal number of qubits required given accuracy ε , namely

$$\mathbf{n} \geq \frac{1}{\log(2)} \log\left(\frac{2}{\pi\sigma^2\varepsilon^2}\right). \quad (4.4)$$

This highlights the quadratic dependence $n = \mathcal{O}(\varepsilon^{-2})$, typical of Monte Carlo-type approximation methods. The dependence on σ^{-2} indicates that narrower Gaussians (smaller σ) require more accuracy blocks, consistent with the broader frequency content of their Fourier transforms. We consider the domain $x \in [-4, 4]$ with 100 uniformly spaced points and optimise the parameters by differential evolution. Figure 3a displays the approximation $f_{n,\boldsymbol{\theta}}^R$ against the true density for $(\sigma, n) = (1, 8)$, with the pointwise absolute error on a logarithmic scale; the empirical RMSE lies below the theoretical L^2 bound $L^1[\hat{f}_\sigma]/\sqrt{n}$ from Theorem 3.6 (noiseless case). Figure 3b plots the measured RMSE against $n \in \{2, 4, 8, 12, 16\}$, together

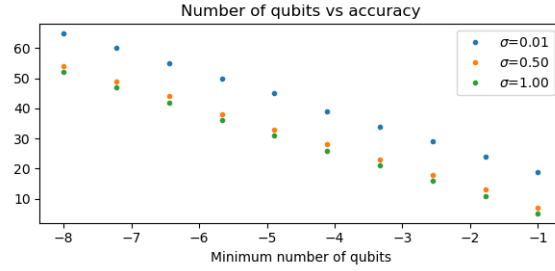


FIGURE 2. Minimal number of required qubits according to (4.4)

with the theoretical $L^1[\hat{f}_\sigma]/\sqrt{n}$ curve and an empirically rescaled $1/\sqrt{n}$ fit; the right panel shows the ratio MAE/ε_n , which lies below 1 throughout, confirming that the bound of Statement 2.1 holds in the finite- n regime. Figure 3c compares the approximation quality for $\sigma \in \{0.5, 1.0, 2.0\}$ for fixed $n = 8$: narrower Gaussians carry larger $L^1[\hat{f}_\sigma] = 1/(\sigma\sqrt{2\pi})$ and incur proportionally larger errors, in quantitative agreement with (4.3).

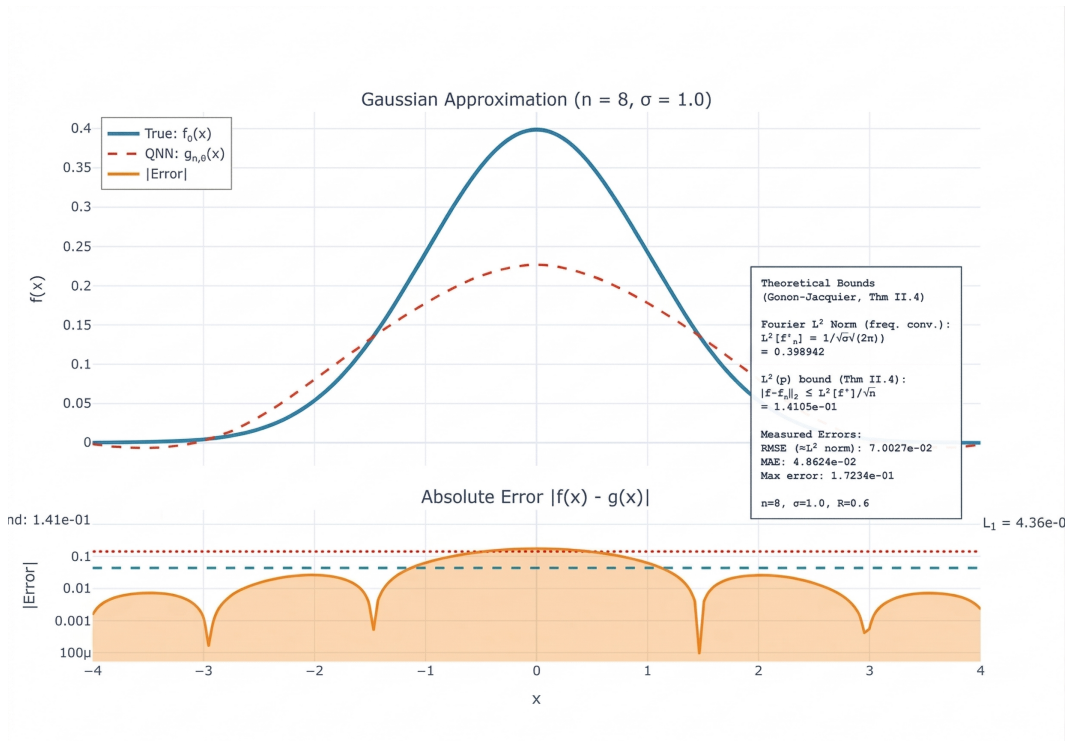
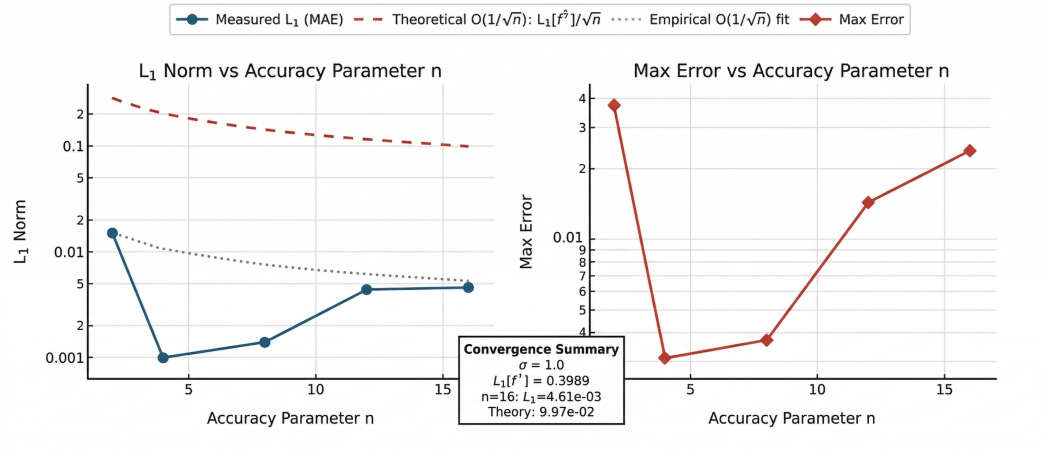
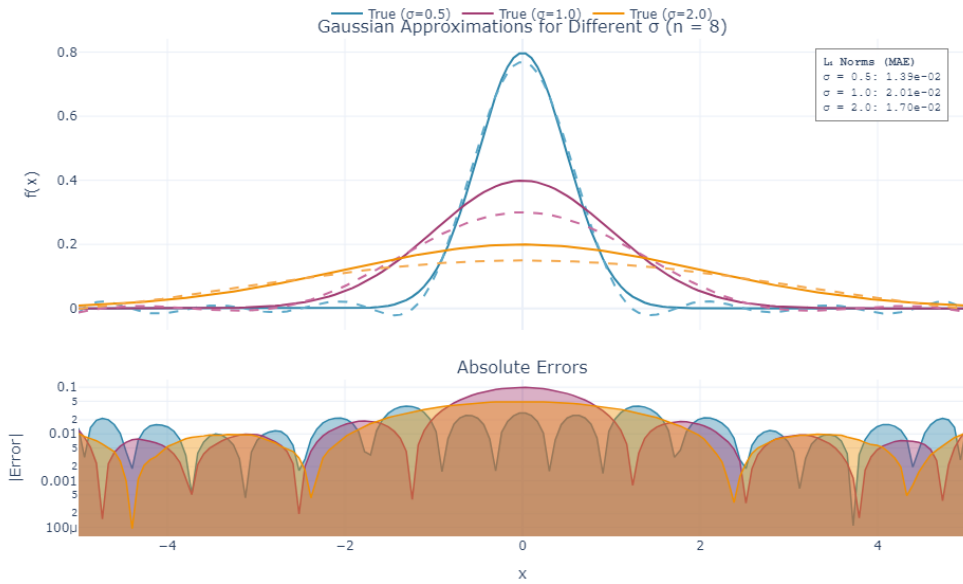
(A) Approximation of f_σ for $(\sigma, n) = (1, 8)$ (top: true vs. QNN; bottom: pointwise $|\text{error}|$, log scale). Dashed: L^2 bound $L^1[\hat{f}_\sigma]/\sqrt{n}$.

FIGURE 3. Gaussian density approximations (Statement 2.1). (Part 1 of 2)



(B) Left: RMSE vs. n (blue circles), theoretical bound (red), $\mathcal{O}(\frac{1}{\sqrt{n}})$ fit (dotted). Right: MAE/ ε_n .

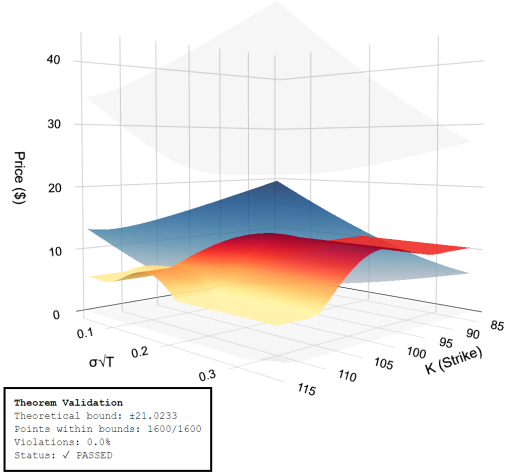


(C) Errors for $\sigma \in \{0.5, 1, 2\}$, $n = 8$ (top: functions; bottom: |error|, log scale).

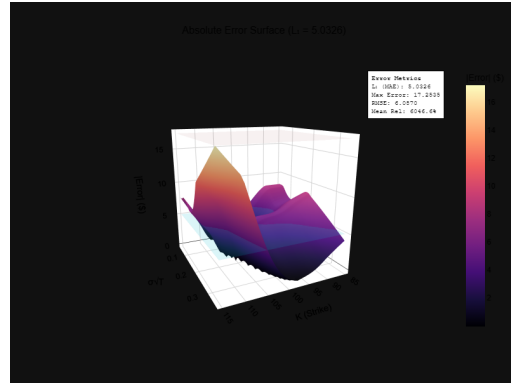
FIGURE 3. Gaussian density approximations (Statement 2.1). (Part 2 of 2)

4.3. Black-Scholes Put option pricing: noiseless regime. Black-Scholes European Put option prices are computed over $S \in [0.8, 1.2]$, $K \in [0.9, 1.1]$, $T \in [0.5, 1.0]$, $r \in$

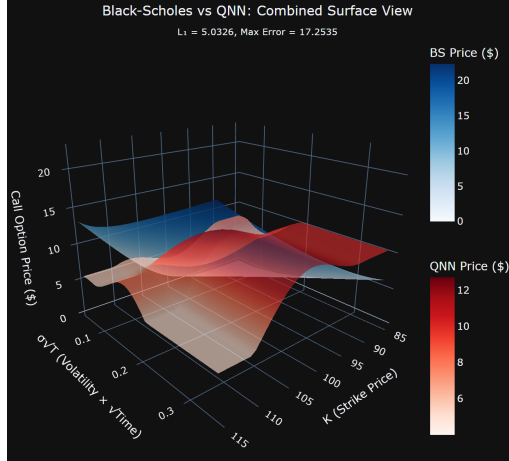
$[0.02, 0.05]$, $\sigma \in [0.1, 0.3]$, all normalised to $[0, 1]^5$ via (4.1). The QNN is trained on the five-dimensional Put-pricing map and evaluated on a 40×40 grid over $(K, \sigma\sqrt{T}) \in [85, 115] \times [0.05, 0.35]$ at fixed $S_0 = 100$, $r = 0.03$. Figure 4a displays the true Black–Scholes surface together with the theoretical error envelope $\pm \mathcal{B}_f(a^*)/\sqrt{n}$ from Example 2.3.3; Figure 4b shows the absolute error surface with horizontal reference planes at the MAE and maximum error. Figure 4c overlays both surfaces and Figure 4d provides a 2D heatmap of $|C_{BS} - f_{n,\theta}^R|$ together with an error histogram. The largest absolute errors concentrate near the deep-in-the-money boundary, consistent with the high-frequency content of $\widehat{\Phi}_1$ in Example 2.3.3.



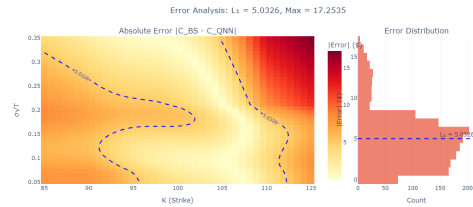
(A) True Black–Scholes (blue) with theoretical error envelope $\pm \mathcal{B}/\sqrt{n}$ (grey glass surfaces).



(B) Absolute error surface $|C_{BS} - f_{n,\theta}^R|$ (Magma colorscale). Cyan plane: MAE; dark-red plane: max error.



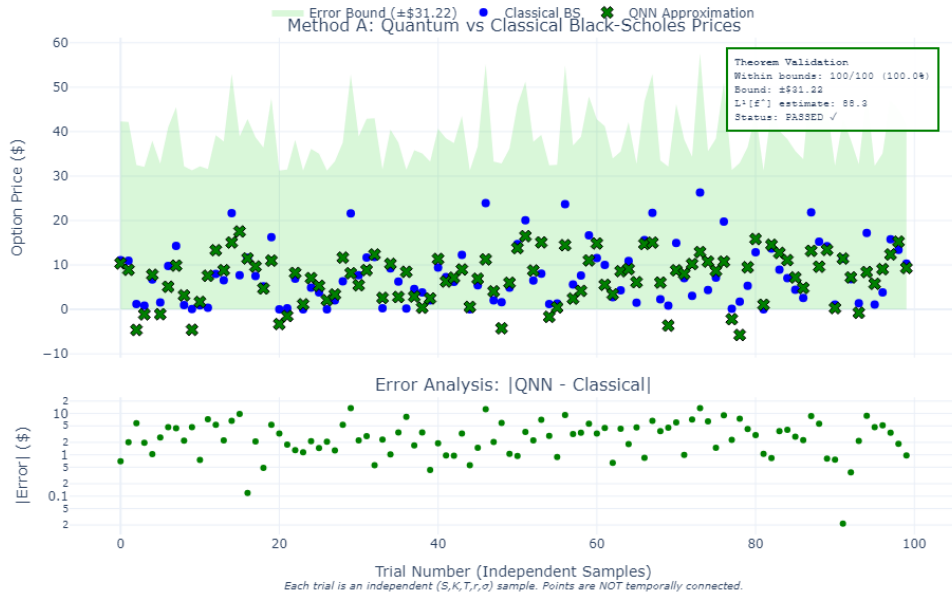
(C) Overlaid surfaces: true Black–Scholes (blue) and QNN approximation (red).



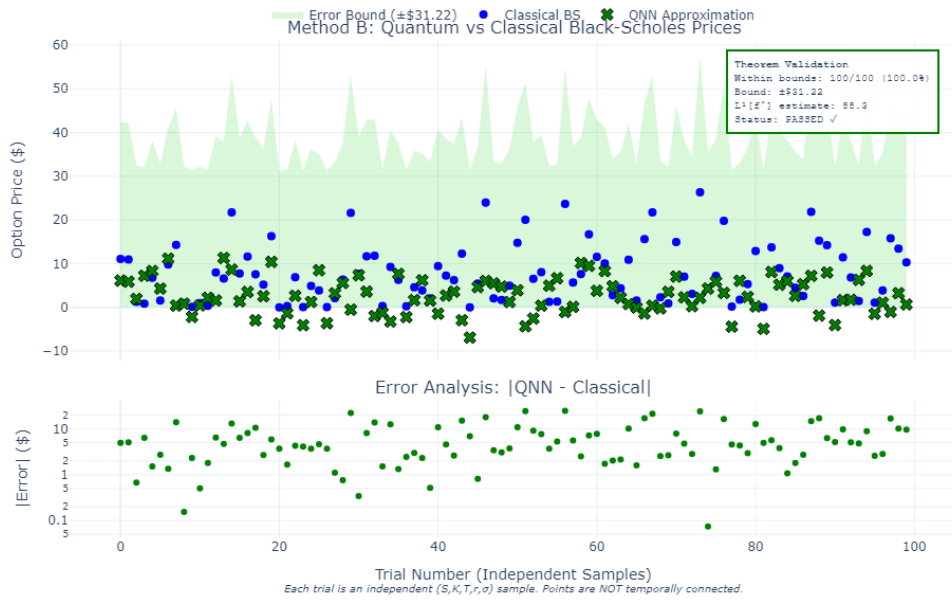
(D) Heatmap of pointwise absolute error (left) and error histogram (right). Errors peak in the deep-in-the-money region.

FIGURE 4. Black–Scholes Put surface approximation (Method A, $n = 8$, $n = 5$ qubits, 40×40 grid, $S_0 = 100$, $r = 0.03$). Theoretical bound from Example 2.3.3.

Figures 5a and 5b compare European Put option prices from Methods A and B against the classical formula on a random test set; the shaded band is the total error bound, and points are coloured green (within bound) or red (outside). Figure 5c presents the four-panel error analysis for Method A: error distribution, approximation error versus n , statistical error versus N_{shots} , and relative error distribution. Figure 6 plots the empirical MAE for Method A against $n \in \{2, 4, 6, 8\}$, alongside the theoretical bound $\varepsilon_n = \frac{L^1[\hat{f}]}{\sqrt{n}} = \frac{\mathfrak{B}}{2\pi\sqrt{n}} S_{\text{max}}$. The ratio MAE/ε_n lies below 1 at all four values of n , confirming that the bound is not merely asymptotic but holds in the finite- n NISQ regime.



(A) Method A: QNN vs. classical BS prices (top) and absolute errors (bottom, log scale). Green: within bound; red: outside.



(B) Method B: same layout as (a). Last-layer optimisation achieves competitive accuracy at substantially lower classical training cost.

FIGURE 5. Per-method noiseless performance. The error bound in (A)–(B) combines the approximation and statistical terms from Corollary 2.4. (C) The error analysis for Method A. (Part 1 of 2)



(c) Error analysis for Method A: error histogram; ε_n vs. n ; statistical error vs. N_{shots} ; relative error histogram.

FIGURE 5. Per-method noiseless performance. The error bound in (A)–(B) combines the approximation and statistical terms from Corollary 2.4. (C) The error analysis for Method A. (Part 2 of 2)

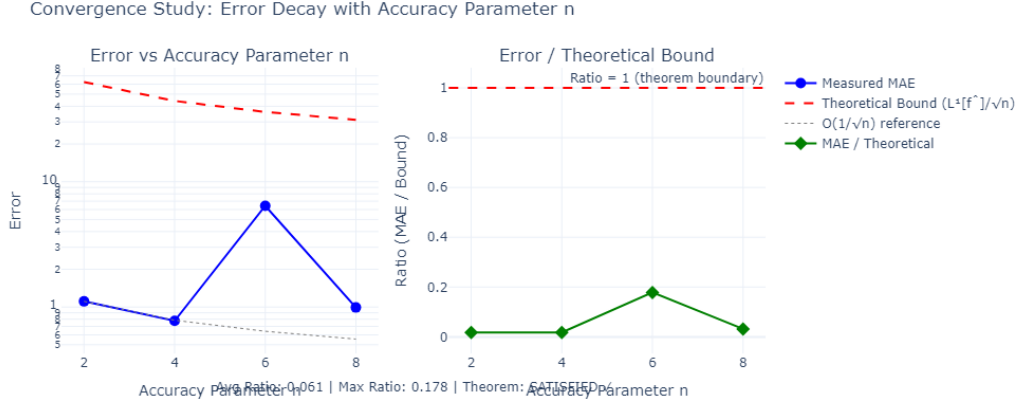
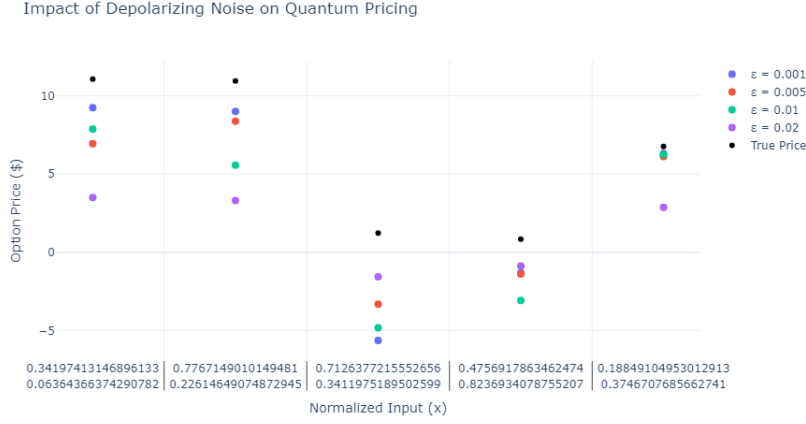
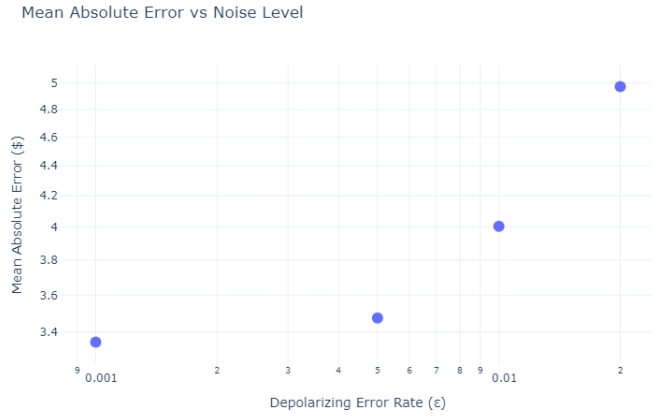


FIGURE 6. Convergence and dimensionality scaling (Method A, noiseless). Left: MAE (blue circles) and sharp bound ε_n (red dashed) on log scale, with $\mathcal{O}(1/\sqrt{n})$ reference (grey dotted). Right: ratio MAE/ε_n . Theoretical bounds from Example 2.3.3 with worst-case parameters $\frac{K_{\max}}{S_{\min}}$, σ_{\min} , T_{\min} .

4.4. Noise simulation. We now consider the depolarisation noise, following Section 3.5. Corollary 3.13 predicts $\tilde{f}_{n,\theta}^R(\mathbf{x}) = \alpha f_{n,\theta}^R(\mathbf{x}) + R(1-\alpha)(1 - \frac{4n}{2^n})$, with $\alpha = (1-\lambda_V)(1-\lambda_U)$, which is validated against exact density-matrix simulation. For each $\varepsilon \in \{0.001, 0.005, 0.01, 0.02\}$, the state $\tilde{\rho}_2^\Delta$ from Proposition 3.9 is constructed explicitly via the projectors $\{\Pi_m\}$ from Section 3.3 ($\Pi_m = \sum_{k=0}^{n-1} |4k+m\rangle\langle 4k+m|$) and compared against `AerSimulator` with a depolarising `NoiseModel`; agreement holds across all 20 test points, validating the theoretical predictions from Section 3. Figure 7a shows QNN outputs for each ε against the classical Black-Scholes reference: increasing ε progressively contracts outputs towards the constant bias $R(1-\alpha)(1 - \frac{4n}{2^n})$ as predicted. Figure 7b plots MAE on a log-log scale against ε ; at $\varepsilon = 0.001$ (near the `ibm_vez` two-qubit error rate $\varepsilon_{2q} = 2.548 \cdot 10^{-3}$) the degradation is modest, while at $\varepsilon = 0.02$ the systematic term $(1-\alpha)\|f\|_{L^2(\mu)}$ of Theorem 3.16 dominates.



(A) Noisy QNN outputs vs. Black-Scholes Put prices (black) across 20 test points. Higher values of ϵ contract the output towards the noise bias $R(1 - \alpha)(1 - \frac{4n}{2^n})$ of Corollary 3.13.



(B) MAE vs. depolarising error rate ϵ (log-log). The growth is consistent with the systematic term $(1 - \alpha)\|f\|_{L^2(\mu)}$ of Theorem 3.16.

FIGURE 7. Depolarising noise simulation ($n = 8$, Method A, $N_{\text{shots}} = 8192$, 20 test points). Density-matrix predictions from Proposition 3.9 agree with **AerSimulator** at all noise levels.

4.5. Hardware execution on `ibm_fez`. Circuits trained by Method A are executed on `ibm_fez` via `SamplerV2` with $N_{\text{shots}} = 8192$ and optimisation level 3 transpilation on 10 test points. Live calibration data yield ϵ as in Table 1; the fidelity factor α defined in (3.7) thus depends on ϵ through λ_U and λ_V and the bound from Proposition 3.19:

$$\epsilon_{\text{total}} = \frac{\alpha L^1[\hat{f}]}{\sqrt{n}} + (1 - \alpha)\|f\|_{L^2(\mu)} + R(1 - \alpha) \left(1 - \frac{4n}{2^n}\right) + 4Rp$$

are computed from these parameters. Figure 8 presents the six-panel hardware analysis. *Panel (a)* compares all three noiseless simulation methods against the classical Black–Scholes formula. *Panel (b)* overlays hardware measurements (with shot-noise error bars from (4.2)) against the depolarising and comprehensive noise model predictions, together with the $\pm\varepsilon_{\text{total}}$ envelope above; the empirical MAE satisfies the bound in all tested instances. *Panel (c)* plots residuals ($P_{\text{hw}} - P_{\text{theory}}$) for each noise model with $\pm\varepsilon_{\text{total}}$ reference lines. *Panel (d)* is a parity plot of theoretical vs. hardware prices; the comprehensive noise model (amplitude damping + phase damping + depolarising) sits closer to the diagonal than the depolarising-only model. *Panel (e)* decomposes $\varepsilon_{\text{total}}$ into approximation, systematic, bias, and readout contributions (bar chart), with the empirical MAE as a horizontal reference; the systematic term $(1 - \alpha)\|f\|_{L^2(\mu)}$ dominates at current hardware noise levels. *Panel (f)* tabulates backend name, shot count, α , total bound, empirical MAE, fraction of test points within the bound, and the Pearson correlation between hardware prices and the comprehensive noise model.



FIGURE 8. Hardware execution on `ibm_fez`.

REFERENCES

- [1] M. ABUGHANEM, *IBM Quantum computers: Evolution, performance, and future directions*, arXiv:2410.00916, (2024).
- [2] J. AFTAB AND H. YANG, *Approximating Korobov functions via quantum circuits*, arXiv:2404.14570, (2024).
- [3] I. AGARWAL, T. L. PATTI, R. A. BRAVO, S. F. YELIN, AND A. ANANDKUMAR, *Extending quantum perceptrons: Rydberg devices, multi-class classification, and error tolerance*, arXiv:2411.09093, (2024).
- [4] A. R. BARRON, *Universal approximation bounds for superpositions of a sigmoidal function*, IEEE Transactions on Information theory, 39 (2002), pp. 930–945.
- [5] J. CUI, P. J. DE BROUWER, S. HERBERT, P. INTALLURA, C. KARGI, G. KORPAS, A. KRAJENBRINK, W. SHOOSMITH, I. WILLIAMS, AND B. ZHENG, *Quantum Monte Carlo integration for simulation-based optimisation*, arXiv:2410.03926, (2024).
- [6] G. CYBENKO, *Approximation by superpositions of a sigmoidal function*, Mathematics of control, signals and systems, 2 (1989), pp. 303–314.
- [7] P. GLASSERMAN, *Monte Carlo Methods in Financial Engineering*, vol. 53, Springer, 2003.
- [8] L. GONON, *Random feature neural networks learn Black-Scholes type PDEs without curse of dimensionality*, Journal of Machine Learning Research, 24 (2023), pp. 1–51.
- [9] L. GONON AND A. JACQUIER, *Universal approximation theorem and error bounds for quantum neural networks and quantum reservoirs*, IEEE Transactions on Neural Networks and Learning Systems, (2025).
- [10] L. GONON, R. MARTÍNEZ-PEÑA, AND J.-P. ORTEGA, *Feedback-driven recurrent quantum neural network universality*, in The Fourteenth International Conference on Learning Representations, 2026.
- [11] K. HORNIK, *Approximation capabilities of multilayer feedforward networks*, Neural networks, 4 (1991), pp. 251–257.
- [12] K. HORNIK, M. STINCHCOMBE, AND H. WHITE, *Multilayer feedforward networks are universal approximators*, Neural networks, 2 (1989), pp. 359–366.
- [13] IBM QUANTUM, *IBM Quantum platform – compute resources*.
- [14] A. N. KOLMOGOROV, *On the representations of continuous functions of many variables by superposition of continuous functions of one variable and addition*, in Dokl. Akad. Nauk USSR, vol. 114, 1957, pp. 953–956.
- [15] K. KRAUS, *General state changes in quantum theory*, Annals of Physics, 64 (1971), pp. 311–335.
- [16] S. KUMAR AND C. M. WILMOTT, *Simulating the non-Hermitian dynamics of financial option pricing with quantum computers*, arXiv:2407.01147, (2024).
- [17] M. LAROCCA, S. THANASILP, S. WANG, K. SHARMA, J. BIAMONTE, P. J. COLES, L. CINCIO, J. R. MCCLEAN, Z. HOLMES, AND M. CEREZO, *Barren plateaus in variational quantum computing*, Nature Reviews Physics, (2025), pp. 1–16.
- [18] M. LESHNO, V. Y. LIN, A. PINKUS, AND S. SCHOCKEN, *Multilayer feedforward networks with a non-polynomial activation function can approximate any function*, Neural networks, 6 (1993), pp. 861–867.
- [19] R. J. LEVEQUE, *Finite Difference Methods for Ordinary and Partial Differential Equations: steady-state and time-dependent problems*, SIAM, 2007.
- [20] A. MANZANO, D. DECHANT, J. TURA, AND V. DUNJKO, *Approximation and generalization capacities of parametrized quantum circuits for functions in Sobolev spaces*, Quantum, 9 (2025), p. 1658.
- [21] V. MARTINEZ, A. ANGRISANI, E. PANKOVETS, O. FAWZI, AND D. STILCK FRANÇA, *Efficient simulation of parametrized quantum circuits under non-unital noise through Pauli backpropagation*, arXiv:2501.13050, (2025).
- [22] A. A. MELE, A. ANGRISANI, S. GHOSH, S. KHATRI, J. EISERT, D. S. FRANÇA, AND Y. QUEK, *Noise-induced shallow circuits and absence of barren plateaus*, arXiv:2403.13927, (2024).
- [23] M. MÖTTÖNEN, J. J. VARTIAINEN, V. BERGHOLM, AND M. M. SALOMAA, *Quantum circuits for general multiqubit gates*, Physical Review Letters, 93 (2004), p. 130502.
- [24] M. A. NIELSEN AND I. L. CHUANG, *Quantum Computation and Quantum Information*, CUP, 2010.
- [25] A. PÉREZ-SALINAS, A. CERVERA-LIERTA, E. GIL-FUSTER, AND J. I. LATORRE, *Data re-uploading for a universal quantum classifier*, Quantum, 4 (2020), p. 226.
- [26] A. PÉREZ-SALINAS, D. LÓPEZ-NÚÑEZ, A. GARCÍA-SÁEZ, P. FORN-DÍAZ, AND J. I. LATORRE, *One qubit as a universal approximant*, Physical Review A, 104 (2021), p. 012405.
- [27] QUANTINUUM, *Quantinuum system model h2 product data sheet*, tech. rep., Quantinuum, 2025.
- [28] M. RAHMAN AND J. ZHUANG, *NQNN: Noise-aware quantum neural network for medical image analysis*, in Medical Image Computing and Computer Assisted Intervention – MICCAI 2025, 2025.

- [29] S. RAMOS-CALDERER, A. PÉREZ-SALINAS, D. GARCÍA-MARTÍN, C. BRAVO-PRIETO, J. CORTADA, J. PLANAGUMA, AND J. I. LATORRE, *Quantum unary approach to option pricing*, Physical Review A, 103 (2021), p. 032414.
- [30] RIGETTI COMPUTING, *Rigetti computing reports on its Q2 2025 financial results*, August 2025.
- [31] ———, *Rigetti reports it halves two-qubit gate error rate*, July 2025.
- [32] K.-I. SATO, *Lévy Processes and Infinitely Divisible Distributions*, vol. 68, CUP, 1999.
- [33] W. SCHERER, *Mathematics of Quantum Computing*, vol. 11, Springer, 2019.
- [34] M. SCHULD, R. SWEKE, AND J. J. MEYER, *Effect of data encoding on the expressive power of variational quantum-machine-learning models*, Physical Review A, 103 (2021), p. 032430.
- [35] N. STAMATOPOULOS, D. J. EGGER, Y. SUN, C. ZOUFAL, R. ITEN, S. WOERNER, AND W. BRAINE, *Option pricing using quantum computers*, Quantum, 4 (2020), p. 291.
- [36] H. WANG, J. GU, Y. DING, Z. LI, F. CHONG, D. Z. PAN, AND S. HAN, *RoQNN: Noise-aware training for robust quantum neural networks*, openreview.net/forum?id=wwIBobGFj2V, (2021).
- [37] H. WANG, J. GU, Y. DING, Z. LI, F. T. CHONG, D. Z. PAN, AND S. HAN, *QuantumNAT: quantum noise-aware training with noise injection, quantization and normalization*, in Proceedings of the 59th ACM/IEEE design automation conference, 2022, pp. 1–6.
- [38] S. WANG, E. FONTANA, M. CEREZO, K. SHARMA, A. SONE, L. CINCIO, AND P. J. COLES, *Noise-induced barren plateaus in variational quantum algorithms*, Nature Communications, 12 (2021), p. 6961.
- [39] D. YAROTSKY, *Error bounds for approximations with deep ReLU networks*, Neural networks, 94 (2017), pp. 103–114.
- [40] Z. YU, Q. CHEN, Y. JIAO, Y. LI, X. LU, X. WANG, AND J. YANG, *Non-asymptotic approximation error bounds of parameterized quantum circuits*, Advances in NeurIPS, 37 (2024), pp. 99089–99127.

SCHOOL OF COMPUTER SCIENCE, UNIVERSITY OF ST. GALLEN AND DEPARTMENT OF MATHEMATICS,
IMPERIAL COLLEGE LONDON

Email address: `l.gonon@imperial.ac.uk`

DEPARTMENT OF MATHEMATICS, IMPERIAL COLLEGE LONDON

Email address: `a.jacquier@imperial.ac.uk`

DEPARTMENT OF COMPUTING, IMPERIAL COLLEGE LONDON

Email address: `marcel.mordarski25@imperial.ac.uk`